



<http://www.diva-portal.org>

## Postprint

This is the accepted version of a paper published in *Journal of the American Chemical Society*. This paper has been peer-reviewed but does not include the final publisher proof-corrections or journal pagination.

Citation for the original published paper (version of record):

Wilson, S., Kroll, T., Decreau, R., Hocking, R., Lundberg, M. et al. (2013)  
Iron L-edge X-ray Absorption Spectroscopy of Oxy-Picket Fence Porphyrin: Electronic  
Structure of the Fe-O<sub>2</sub> Bond.  
*Journal of the American Chemical Society*, 135(3): 1124-1136  
<http://dx.doi.org/10.1021/ja3103583>

Access to the published version may require subscription.

N.B. When citing this work, cite the original published paper.

Permanent link to this version:

<http://urn.kb.se/resolve?urn=urn:nbn:se:uu:diva-198495>

# Iron L-edge X-ray Absorption Spectroscopy of Oxy-Picket Fence Porphyrin: Experimental Insight into Fe-O<sub>2</sub> Bonding

Samuel A. Wilson,<sup>†</sup> Thomas Kroll,<sup>†</sup> Richard A. Decreau,<sup>†,A</sup> Rosalie K. Hocking,<sup>†,B</sup> Marcus Lundberg,<sup>†,C</sup>  
Britt Hedman,<sup>‡,\*</sup> Keith O. Hodgson,<sup>†,‡,\*</sup> and Edward I. Solomon<sup>†,‡,\*</sup>

<sup>†</sup>*Department of Chemistry, Stanford University, Stanford, CA 94305, U.S.A.*

<sup>‡</sup>*Stanford Synchrotron Radiation Lightsource, SLAC National Accelerator Laboratory, Stanford University,  
Menlo Park, CA 94025-7015, U.S.A.*

\*Corresponding authors: hedman@slac.stanford.edu, hodgson@slac.stanford.edu, and edward.solomon@stanford.edu.

---

*KEYWORDS: Iron L-edge, X-ray Absorption Spectroscopy, Oxy-hemoglobin, Picket Fence Porphyrin, Electronic Structure.*

---

### \*\*\*Present Addresses\*\*\*

<sup>A</sup>*Department of Chemistry, Université de Bourgogne, Institut de Chimie Moléculaire, 9 Av. Alain Savary, Sciences Mirande, 21078 Dijon, France.*

<sup>B</sup>*School of Chemistry and Monash Centre for Synchrotron Science, Clayton, Australia, 3800*

<sup>C</sup>*Department of Chemistry, Ångström laboratory, Uppsala University, Box 518, SE-751 20 Uppsala, Sweden*

## **Abstract**

The electronic structure of the Fe–O<sub>2</sub> center in oxy-hemoglobin and oxy-myoglobin is a long-standing issue in the field of bioinorganic chemistry. Spectroscopic studies have been complicated by the highly delocalized nature of the porphyrin and calculations require interpretation of multi-determinant wavefunctions for a highly covalent metal site. Here, iron L-edge X-ray absorption spectroscopy (XAS), interpreted using a valence bond configuration interaction (VBCI) multiplet model, is applied to directly probe the electronic structure of the iron in the biomimetic Fe–O<sub>2</sub> heme complex [Fe(pfp)(1-MeIm)O<sub>2</sub>] (pfp = *meso*-tetra( $\alpha, \alpha, \alpha, \alpha$ -*o*-pivalamidophenyl)porphyrin or TpivPP). This method allows separate estimates of  $\sigma$ -donor,  $\pi$ -donor, and  $\pi$ -acceptor interactions through ligand to metal charge transfer (LMCT) and metal to ligand charge transfer (MLCT) mixing pathways. The L-edge spectrum of [Fe(pfp)(1-MeIm)O<sub>2</sub>] is further compared to those of [Fe<sup>II</sup>(pfp)(1-MeIm)<sub>2</sub>], [Fe<sup>II</sup>(pfp)], and [Fe<sup>III</sup>(tpp)(ImH)<sub>2</sub>]Cl (tpp = *meso*-tetraphenylporphyrin) which have Fe<sup>II</sup>  $S = 0$ , Fe<sup>II</sup>  $S = 1$  and Fe<sup>III</sup>  $S = 1/2$  ground states, respectively. These serve as references for the three possible contributions to the ground state of oxy-pfp. The Fe–O<sub>2</sub> pfp site is experimentally determined to have both significant  $\sigma$ -donation and a strong  $\pi$ -interaction of the O<sub>2</sub> with the iron, with the latter having implications with respect to the spin polarization of the ground state.

## 1. Introduction

Oxy-hemoglobin (Hb) and oxy-myoglobin (Mb) are dioxygen transport and storage metalloproteins located in red blood cells and aerobic muscle tissue.<sup>1-4</sup> Both of these proteins feature an iron heme active site in which the deoxygenated form has a high-spin ( $S = 2$ ) ferrous center that becomes diamagnetic upon  $O_2$  binding.<sup>5,6</sup> While the end-on Fe– $O_2$  geometric structure of oxy-hemoglobin and oxy-myoglobin are well known,<sup>7-9</sup> there has been a long standing discussion, recently summarized by Shaik et. al.,<sup>10</sup> concerning the electronic structure of the Fe– $O_2$  bond. Three limiting descriptions of the Fe– $O_2$  bond have generally been considered: a low-spin ( $S = 0$ ) ferrous center with singlet  $O_2$ , as initially suggested by Pauling;<sup>6,11</sup> a low-spin ( $S = 1/2$ ) ferric center, antiferromagnetically coupled to an  $O_2^-$  doublet as proposed by Weiss;<sup>12</sup> and an intermediate-spin ( $S = 1$ ) ferrous site, antiferromagnetically coupled to triplet  $O_2$ , referred to as the Ozone model of McClure, Harcourt, and Goddard [(Scheme 1)].<sup>13-16</sup>

An array of different spectroscopic and computational methods have been used in attempts to address the nature of the Fe– $O_2$  bond in oxy-hemoglobin and oxy-myoglobin.<sup>3,10,17-28</sup> The heme unit is highly covalent, with significant delocalization of the iron 3d electrons into the porphyrin  $\pi^*$  system.<sup>29-34</sup> The ability of the heme to redistribute the charge and spin density of the iron plays an essential role in the formation and stabilization of a variety of intermediates required for biological function.<sup>35</sup> However, this delocalization also complicates the ability of many spectral methods to evaluate the electronic structure of the iron.<sup>36</sup> Furthermore, the presence of several energetically accessible spin states, can make computational evaluations challenging.<sup>22-26</sup>

Iron L-edge X-ray absorption spectroscopy (XAS) is a direct probe of the electronic structure of a metal center in a highly covalent environment, as in a porphyrin.<sup>36</sup> The L-edge spectrum involves an electric dipole allowed  $2p \rightarrow 3d$  transition, and since the  $2p$  orbital is localized on the iron, the intensity of the L-edge quantifies the amount of metal d-character in the unoccupied valence orbitals of the complex.<sup>37</sup> As unoccupied d-character (i.e. L-edge intensity) increases or decreases, the  $Z_{\text{eff}}$  of the iron changes accordingly as does the energy of the L-edge transition. Ligand donor interactions through ligand to metal charge transfer (LMCT) configuration interaction (CI) decrease the amount of d-character while ligand acceptor interactions through metal to ligand charge transfer (MLCT), backbonding, shifts occupied metal character into the ligand  $\pi^*$  orbitals, which results in increased L-edge intensity.<sup>36,38</sup>

The iron L-edge spectrum is split into two main spectroscopic features. These arise from the presence of a 2p core hole which has a large spin-orbit interaction that gives the  $L_3$  ( $J = 3/2$ ) and  $L_2$  ( $J = 1/2$ ) peaks. These peaks are energy-split by  $\sim 10\text{--}15$  eV with an intensity ratio of  $\sim 2:1$ . Furthermore, the  $2p \rightarrow 3d$  transitions produce  $2p^5 3d^{N+1}$  final states that are split in energy by p-d and d-d electron repulsion and ligand field effects. In the low-spin iron heme systems studied here, the ligand field splitting is large and separates the  $d\pi$  from the  $d\sigma$  holes by several eV. To these are added the differential orbital covalency (DOC),<sup>37</sup> the difference in covalency for the  $d\pi$  and  $d\sigma$  levels, which influences the intensity pattern of the final state multiplets. Note that in heme systems the  $\sigma$ -covalency in  $D_{4h}$  further splits into  $a_{1g}$  ( $d_z^2$ ) and  $b_{1g}$  ( $d_{x^2-y^2}$ ) components. Thus, covalency affects both the L-edge intensity and its distribution. This is included in the analysis of the L-edge spectrum through LMCT configuration interaction for donation and MLCT configuration interaction for backbonding.

In this investigation, iron L-edge XAS is used to study oxy-picket fence porphyrin<sup>7,39</sup> (pfp = *meso*-tetra( $\alpha, \alpha, \alpha, \alpha$ -*o*-pivalamidophenyl)porphyrin or TpivPP), the first structurally defined reversible dioxygen binding heme complex that models oxy-hemoglobin and oxy-myoglobin.<sup>7,8</sup> This complex exhibits similar vibrational and Mössbauer parameters to those of the proteins, and first demonstrated that dioxygen was bound to iron in an end-on fashion.<sup>7,8</sup> Also included are the L-edge spectra of  $[\text{Fe}^{\text{II}}(\text{pfp})(1\text{-MeIm})_2]$  (1-MeIm = 1-methylimidazole) a low-spin ( $S = 0$ ) ferrous heme complex as in the Pauling model,<sup>6,11</sup> ferrous  $[\text{Fe}^{\text{II}}(\text{pfp})]$  which has no axial ligands and thus has an intermediate-spin ( $S = 1$ ) as in the Ozone model of McClure, Harcourt, and Goddard,<sup>13-16</sup>  $[\text{Fe}^{\text{II}}(\text{pfp})(1\text{-MeIm})(\text{CO})]$  which is a well defined low-spin ( $S = 0$ ) ferrous complex with significant  $\pi$ -backbonding, and  $[\text{Fe}^{\text{III}}(\text{tpp})(\text{ImH})_2]\text{Cl}$  (tpp = *meso*-tetraphenylporphyrin, ImH = imidazole), a low-spin ( $S = 1/2$ ) ferric complex as considered by Weiss.<sup>12</sup>

This study experimentally determines the  $\sigma$  and  $\pi$  contributions to the bonding in each of these complexes. In particular the  $d_z^2$  and  $d_{x^2-y^2}$   $d\sigma$  splitting is evaluated to directly determine the  $d\pi$ -interaction of the iron with the  $\pi^*$  orbital of  $\text{O}_2$ , where in the Pauling model this bonding is innocent while in the Weiss model the spins localize on the  $\text{O}_2$  and the iron.

## 2. Materials and Methods

### 2.1. Samples

The compounds  $[\text{Fe}^{\text{II}}(\text{pfp})(1\text{-MeIm})_2]$ ,  $[\text{Fe}^{\text{II}}(\text{pfp})(1\text{-MeIm})(\text{CO})]$ ,  $[\text{Fe}(\text{pfp})(1\text{-MeIm})\text{O}_2]$ ,  $[\text{Fe}^{\text{II}}(\text{pfp})]$ ,  $[\text{Fe}^{\text{II}}(\text{tpp})(\text{ImH})_2]$ , and  $[\text{Fe}^{\text{III}}(\text{tpp})(\text{ImH})_2]\text{Cl}$  were synthesized and characterized according to published methods.<sup>7,39-41</sup> Prior to data collection, all samples were maintained in a nitrogen inert atmosphere glovebox. For the L-edge measurements the samples were spread across double-sided adhesive conductive graphite tape, attached to a copper paddle, and transferred to a nitrogen glovebag for loading into the ultra-high vacuum (UHV) experimental chamber.

### 2.2. XAS Data Collection and Reduction

X-ray absorption spectra were collected at the Stanford Synchrotron Radiation Lightsource (SSRL) on beamline 10-1 under ring operating conditions of 100–350 mA and 3 GeV. The radiation was dispersed using a spherical grating monochromator set at 1000 lines/mm with 20  $\mu\text{m}$  entrance and exit slits for a resolution of  $\sim 0.1$  eV. Data for all samples were recorded using a UHV beamline end-station maintained at  $5.0 \times 10^{-9}$  Torr with samples aligned at  $45^\circ$  to the incident beam as described previously.<sup>37,42</sup>

L-edge spectra were measured by total electron yield with a Galileo 4716 channeltron electron multiplier aligned parallel to the sample surface normal and  $45^\circ$  relative to the incident beam. The signal flux ( $I_1$ ) was normalized by the photocurrent of an upstream gold-grid reference monitor ( $I_0$ ). The photon energy was calibrated to 708.5 and 720.1 eV for the  $L_3$ - and  $L_2$ -edge, respectively, of powdered  $\alpha\text{-Fe}_2\text{O}_3$  (hematite  $< 5 \mu\text{M}$ ) run before and after each set of sample scans. Data were collected over the range of 670 to 830 eV to allow for proper normalization,<sup>37</sup> with a step size of 0.1 eV employed from 700 to 730 eV, and 0.5 eV for remaining regions of the spectrum.

A single scan of the L-edge spectrum took an average of  $\sim 10$  min, with  $\sim 4$  min over the 700–730 eV energy region. Four to six scans were averaged together to obtain a final data set with a high signal to noise ratio. Photo-reduction was only observed in the ferric reference compound  $[\text{Fe}^{\text{III}}(\text{tpp})(\text{ImH})_2]\text{Cl}$ . However,  $[\text{Fe}^{\text{II}}(\text{pfp})(1\text{-MeIm})_2]$ ,  $[\text{Fe}^{\text{II}}(\text{pfp})(1\text{-MeIm})(\text{CO})]$ ,  $[\text{Fe}(\text{pfp})(1\text{-MeIm})\text{O}_2]$ , and  $[\text{Fe}^{\text{II}}(\text{tpp})(\text{ImH})_2]$  exhibited an increased rate of pumping decay when exposed to X-ray radiation. As a result, all samples were kept cold using a liquid helium cryostat

with measurements taken at temperatures between 220–240 K. Maintaining the samples at lower temperatures prevented decay either by pumping or photo-reduction, and allowed collection of reproducible high-quality data.

A function of the form: absorption ( $\chi$ ) =  $[\tan^{-1}(k(\text{energy} - I_1) + \pi/2)(2/3(1/\pi))] + [\tan^{-1}(k(\text{energy} - I_2) + \pi/2)(1/3)(1/\pi)]$ , with  $k = 0.295$ , obtained by experimental fit,<sup>37,43</sup> and  $I_2 = I_1 + 12.3$  eV (energy split by spin-orbit coupling), was used to model the L<sub>3</sub>- and L<sub>2</sub>-edge jumps.<sup>37</sup> The energy of the arctangent was estimated on the basis of the fit to the L-edge experiment.<sup>36-38,44-46</sup>

### 2.3. VBCI Multiplet Simulations

Ligand field multiplet calculations were performed using the multiplet model implemented by Thole,<sup>47</sup> with the atomic theory developed by Cowan,<sup>48</sup> and the crystal field symmetry interactions described by Butler,<sup>49</sup> which includes both Coulomb interactions and spin-orbit coupling for each sub-shell.<sup>50,51</sup> To simulate the spectra, the Slater-Condon-Shortley parameters  $F_i$  and  $G_i$  were reduced to 80% of their Hartree-Fock calculated values in order to account for the over-estimation of electron-electron repulsion found in the calculations of the free ion ( $\kappa = 0.8$ ).<sup>50,52,53</sup> The final multiplet spectrum is calculated from the sum of all transitions for electrons excited from an iron 2p into the 3d unoccupied orbitals.<sup>54</sup> In the ligand field limit, the ground state is approximated by a single electronic configuration  $d^N$  split in energy by a ligand field potential in  $D_{4h}$  symmetry, which is defined by the parameters, 10Dq, Ds, and Dt. The relationship between the orbital energies and the ligand field parameters is:  $b_{1g}(d_{x^2-y^2}) = 6Dq + 2Ds - 1Dt$ ,  $a_{1g}(d_z^2) = 6Dq - 2Ds - 6Dt$ ,  $b_{2g}(d_{xy}) = -4Dq + 2Ds - 1Dt$ , and  $e_g(d_{xz/yz}) = -4Dq - 1Ds + 4Dt$ . Covalent mixing of the valence metal d-orbitals with the valence ligand p-orbitals is simulated using a charge transfer model in which ligand to metal charge transfer adds a  $d^{N+1}\underline{L}$  configuration ( $\underline{L}$  = ligand hole) at an energy ( $\Delta$ ) above the  $d^N$  ground state. These two states couple through configuration interaction, which is introduced by the mixing term  $T_i = \langle 3d^N | h | d^{N+1}\underline{L} \rangle$ , where  $h$  is the molecular Hamiltonian operator and  $T_i$  is proportional to the metal-ligand overlap for each of the  $i$  symmetry blocks. In the case of a donor ligand system, the ground and LMCT states are defined by  $\Psi_{GS,B} = \alpha_1|3d^N\rangle + \beta_1|3d^{N+1}\underline{L}\rangle$  and  $\Psi_{GS,AB} = \beta_1|3d^N\rangle - \alpha_1|3d^{N+1}\underline{L}\rangle$ , respectively, and the excited states are defined as  $\Psi_{ES,B} = \alpha_2|2p^5 3d^{N+1}\rangle + \beta_2|2p^5 3d^{N+2}\underline{L}\rangle$  and  $\Psi_{ES,AB} = \beta_2|2p^5 3d^{N+1}\rangle - \alpha_2|2p^5 3d^{N+2}\underline{L}\rangle$ . Here the coefficients  $\alpha_1$ ,  $\alpha_2$ ,  $\beta_1$ , and  $\beta_2$

are functions of  $T$  and  $\Delta$  for the ground state, and  $T$  and  $\Delta'$  for the final state, where  $\Delta' = \Delta + U - Q$ , where  $U$  is the 3d–3d electron repulsion and  $Q$  the 2p–3d repulsion. To limit the number of variables,  $Q - U$  was maintained between 1.0–1.2 eV.<sup>55</sup> Additionally, the ligand field parameters (10Dq, Ds, and Dt),  $T$ , and  $\Delta$  were fixed in the ground and final state. Metal to ligand charge transfer was included by introductions of a third configuration defined as  $d^{N-1}L^-$ , separated from the ground state by an energy,  $\Delta_{BB}$  ( $\Delta$ -backbonding). The resultant ground-state wave functions are thus combinations of three configurations,  $3d^{N-1}L^-$ ,  $3d^N$ , and  $3d^{N+1}\underline{L}$ .<sup>36,38</sup>

To simulate the L-edge spectra, parameters were initially chosen on the basis of previous fits<sup>36</sup> and constraints obtained by density functional theory (DFT) results (*vide infra*). Parameters that determine the energy separations between the  $d^{N-1}L^-$ ,  $d^N$ , and  $d^{N+1}\underline{L}$  configurations in the ground state ( $\Delta$  and  $\Delta_{BB}$ ) were obtained from the program parameters, where EG1 = 0, EG2 =  $-\Delta_{BB}$ , and EG3 =  $\Delta - \Delta_{BB}$ , and fixed in the final state where EF1 = 0, EF2 =  $-\Delta_{BB} - Q + U$  and EF3 =  $\Delta - \Delta_{BB} - 2(Q - U)$ .

In order to get covalency values for each of the symmetry blocks, a DOC projection method was applied that uses the multiplets<sup>48,49</sup> to distribute the intensity into its different symmetry components via virtual  $4s \rightarrow 4p$  transitions.<sup>37</sup> These projected values were then degeneracy weighted and calibrated to the experimental total intensity to extract the DOC. The final simulated fit to each spectrum was evaluated on the basis of simulated spectral shape relative to the data, the relative weights of the three ground configurations ( $d^{N-1}L^-$ ,  $d^N$ , and  $d^{N+1}\underline{L}$ ), the projected intensities into each of the symmetry blocks, and its agreement with other spectroscopic and computational results.

## 2.4. DFT Calculations

The starting structures for  $[\text{Fe}^{\text{II}}(\text{pfp})(1\text{-MeIm})_2]$ ,  $[\text{Fe}^{\text{II}}(\text{pfp})(1\text{-MeIm})(\text{CO})]$ ,  $[\text{Fe}^{\text{II}}(\text{pfp})]$ , and  $[\text{Fe}^{\text{III}}(\text{pfp})(1\text{-MeIm})_2]^+$  were taken from, or modified from, the crystal structure of  $[\text{Fe}^{\text{II}}(\text{pfp})(1\text{-MeIm})_2]$ .<sup>56</sup>  $[\text{Fe}^{\text{II}}(\text{tpp})(\text{ImH})_2]$  and  $[\text{Fe}^{\text{III}}(\text{tpp})(\text{ImH})_2]^+$  were taken from the crystal structure of  $[\text{Fe}(\text{tpp})(\text{ImH})_2]\text{Cl}$ .<sup>41</sup>  $[\text{Fe}(\text{pfp})(1\text{-MeIm})\text{O}_2]$  was taken directly from its crystal structure.<sup>57</sup>

Ground state DFT calculations and geometry optimizations were performed with Gaussian 09<sup>58</sup> using the unrestricted GGA exchange functional of Becke<sup>59</sup> with the non-local correlation of Perdew<sup>60</sup> 1986 (UBP86) with the 6-311G\* basis set on iron and the smaller 6-31G\* basis set on all other atoms. Several other basis sets and functionals were tested, however, the above combination yielded results consistent with previous L-edge studies<sup>36-38,44,46</sup> which

used UBP86 in the Amsterdam Density Functional (ADF) modeling suite.<sup>61</sup> Frequency calculations on the final optimized geometries contained only real frequencies. Mulliken populations were analyzed using QMForge<sup>62</sup> and orbital diagrams were plotted with gOpenMol.<sup>63,64</sup>

### 3. Results

L-edge XAS data were collected on low-spin ferrous ( $S = 0$ )  $[\text{Fe}^{\text{II}}(\text{pfp})(1\text{-MeIm})_2]$  and  $[\text{Fe}^{\text{II}}(\text{pfp})(1\text{-MeIm})(\text{CO})]$ , intermediate-spin ( $S = 1$ ) ferrous  $[\text{Fe}^{\text{II}}(\text{pfp})]$ , low-spin ferric ( $S = 1/2$ )  $[\text{Fe}^{\text{III}}(\text{tpp})(\text{ImH})_2]\text{Cl}$ , and low-spin ( $S = 0$ )  $[\text{Fe}(\text{pfp})(1\text{-MeIm})\text{O}_2]$ , under ultra-high vacuum using electron yield detection. Under these experimental conditions at room temperature  $[\text{Fe}^{\text{II}}(\text{pfp})(1\text{-MeIm})_2]$ ,  $[\text{Fe}^{\text{II}}(\text{pfp})(1\text{-MeIm})(\text{CO})]$ , and  $[\text{Fe}(\text{pfp})(1\text{-MeIm})\text{O}_2]$  exhibited substantial degradation by the loss of a labile axial ligand. Thus, a control experiment was performed in which the samples were left at room-temperature and pumped for one week at  $5 \times 10^{-9}$  Torr. For each complex, this procedure resulted in a 5-coordinate pumped species with a high-spin ( $S = 2$ ) L-edge spectrum. For  $[\text{Fe}^{\text{II}}(\text{pfp})(1\text{-MeIm})_2]$  this effect is shown in [Figure 1] with the pumped 5-coordinate species in light blue. Analogous comparisons for  $[\text{Fe}^{\text{II}}(\text{pfp})(1\text{-MeIm})(\text{CO})]$  and  $[\text{Fe}(\text{pfp})(1\text{-MeIm})\text{O}_2]$  are given in SI Figure S1. Although the pumped data are different in both spectral shape and energy from the spectrum of interest (collected at low-temperature), they do overlap the low-energy region of the  $[\text{Fe}^{\text{II}}(\text{pfp})(1\text{-MeIm})_2]$   $L_3$ -edge, from 704–708 eV (Figure 1A). Therefore the low-energy shoulder may contain a small contribution from the associated 5-coordinate pumped species. A final corrected spectrum was thus generated by subtracting increasing percentages of the pumped spectrum, followed by renormalization, until the resultant spectrum became negative (unphysical), Figure 1B. This established an upper limit of contamination (Figure 1C). This procedure yielded a maximum of  $< 15\%$  pumped contaminant in the data for  $[\text{Fe}^{\text{II}}(\text{pfp})(1\text{-MeIm})_2]$  and  $[\text{Fe}(\text{pfp})(1\text{-MeIm})\text{O}_2]$ , and  $< 20\%$  for  $[\text{Fe}^{\text{II}}(\text{pfp})(1\text{-MeIm})(\text{CO})]$  (SI Figure S2).

$[\text{Fe}^{\text{II}}(\text{pfp})(1\text{-MeIm})_2]$  is a 6-coordinate low-spin ( $S = 0$ ) ferrous center in the picket fence porphyrin ligand.<sup>7</sup> The L-edge spectrum of  $[\text{Fe}^{\text{II}}(\text{pfp})(1\text{-MeIm})_2]$  is similar to the L-edge spectrum of previously studied<sup>36</sup>  $[\text{Fe}^{\text{II}}(\text{tpp})(\text{ImH})_2]$  (SI Figure S3) with a single main  $L_3$  feature at 708.2 eV and a smaller high energy shoulder at 710.1 eV (Figure 1C). Together with the  $L_2$ -edge at 720.1 eV, the L-edge of  $[\text{Fe}^{\text{II}}(\text{pfp})(1\text{-MeIm})_2]$  has a total intensity of 38 normalized units,

corresponding to a total metal d-character<sup>37</sup> of 302% in the unoccupied valence orbitals ([Table 1]).

Exchanging the axial 1-MeIm ligand in the picket fence cage with CO gives [Fe(pfp)(1-MeIm)(CO)] [Figure 2A] with the uncorrected data given in SI Figure S1.<sup>7,8</sup> Carbonyl (C≡O) is a strong field ligand with backbonding similar to cyanide (CN<sup>-</sup>).<sup>38</sup> Compared to [Fe<sup>II</sup>(pfp)(1-MeIm)<sub>2</sub>], which is included as a reference in Figure 2 as the dashed line, the L<sub>3</sub>-edge of [Fe<sup>II</sup>(pfp)(1-MeIm)(CO)] is shifted up in energy and intensity to 708.6 eV and 41 normalized units, respectively (Table 1). The L-edge of [Fe<sup>II</sup>(pfp)(1-MeIm)(CO)] also has substantially more intensity in the high-energy L<sub>3</sub> feature at 710.0 eV relative to [Fe<sup>II</sup>(pfp)(1-MeIm)<sub>2</sub>], with a corresponding feature now clearly visible in the L<sub>2</sub>-edge at 722.6 eV. These additional features result from filled metal 3d orbitals backbonding into low lying CO π\* orbitals.<sup>38</sup> In addition, the main L<sub>3</sub> feature has become narrower relative to [Fe<sup>II</sup>(pfp)(1-MeIm)<sub>2</sub>], indicative of the destabilization of the d<sub>z<sup>2</sup></sub> orbital associated with the strong σ-donor character of CO.

The L-edge spectrum of [Fe(pfp)(1-MeIm)O<sub>2</sub>], Figure 2B, is very similar to that of [Fe<sup>II</sup>(pfp)(1-MeIm)<sub>2</sub>] (dashed). The L<sub>3</sub>-edge is shifted up slightly in energy (0.1 eV) to 708.3 eV compared to [Fe<sup>II</sup>(pfp)(1-MeIm)<sub>2</sub>], with a total intensity of 39 normalized units corresponding to 310% total d-character in the unoccupied valence orbitals. [Fe(pfp)(1-MeIm)O<sub>2</sub>] also exhibits similar spectral changes as found for [Fe<sup>II</sup>(pfp)(1-MeIm)(CO)] (Figure 2A) with the main L<sub>3</sub> feature being slightly narrower than [Fe<sup>II</sup>(pfp)(1-MeIm)<sub>2</sub>], and with increased intensity in the high-energy feature at 710.2 eV.

The L-edge spectrum of intermediate-spin [Fe<sup>II</sup>(pfp)], Figure 2C, is very different from that of the low-spin [Fe<sup>II</sup>(pfp)(1-MeIm)<sub>2</sub>], with a much broader low-energy L<sub>3</sub> peak that exhibits a unique spectral shape with three features at 705.7, 706.5, and 708.1 eV. The main 708.1 eV feature is slightly lower in energy by 0.1 eV compared to that of [Fe<sup>II</sup>(pfp)(1-MeIm)<sub>2</sub>], and the total intensity has increased to 40 normalized units (Table 1) representing 318% total metal d-character in the unoccupied valence orbitals. This spectral shape reflects a large energy decrease in the d<sub>z<sup>2</sup></sub> orbital relative to the d<sub>x<sup>2</sup>-y<sup>2</sup></sub>, due to the lack of axial ligands, and additional multiplet effects as a result of the *S* = 1 intermediate-spin ground state (see VBCI simulations in section 4.2).

In picket fence porphyrin, an analogous low-spin (*S* = 1/2) ferric bis-imidazole complex, [Fe<sup>III</sup>(pfp)(1-MeIm)<sub>2</sub>]<sup>+</sup>, has not been well defined. Therefore, data were re-collected on [Fe<sup>III</sup>(tpp)(ImH)<sub>2</sub>]Cl<sup>41</sup> (Figure 2D) at higher resolution relative to reference 36 to compare with

the higher-resolution pfp spectra presented here.<sup>36,41</sup> Note that the L-edge spectra of  $[\text{Fe}^{\text{II}}(\text{pfp})(1\text{-MeIm})_2]$  and  $[\text{Fe}^{\text{II}}(\text{tpp})(\text{ImH})_2]$  are essentially equivalent (SI Figure S3), and therefore  $[\text{Fe}^{\text{III}}(\text{tpp})(\text{ImH})_2]\text{Cl}$  serves as a reasonable reference. Relative to  $[\text{Fe}^{\text{II}}(\text{pfp})(1\text{-MeIm})_2]$ , the L-edge spectrum of  $[\text{Fe}^{\text{III}}(\text{tpp})(\text{ImH})_2]\text{Cl}$  is shifted to higher energy by 1.0 eV with a maximum at 709.2 eV and an increase in the total intensity to 46 normalized units, or 365% metal d-character in the unoccupied valence orbitals, both of which reflect the increase in  $Z_{\text{eff}}$  of a ferric relative to a ferrous complex. However, the most noticeable difference is the formation of the prominent low-energy feature at 706.1 eV. This feature has been assigned as the 2p transition to the 3d  $t_2^5 d\pi$  hole<sup>36-38</sup> and is a clear characteristic feature of a low-spin ferric species. It is important to note that  $[\text{Fe}(\text{pfp})(1\text{-MeIm})\text{O}_2]$  (Figure 2B) lacks this feature in its L-edge XAS spectrum (SI Figure S4).

## 4. Analysis

### 4.1. DFT Calculations of Reference Complexes

DFT calculations on  $[\text{Fe}^{\text{II}}(\text{pfp})(1\text{-MeIm})_2]$ ,  $[\text{Fe}^{\text{II}}(\text{pfp})(1\text{-MeIm})(\text{CO})]$ ,  $[\text{Fe}^{\text{II}}(\text{pfp})]$  and  $[\text{Fe}^{\text{III}}(\text{pfp})(1\text{-MeIm})_2]^+$  are presented here for correlation to the VBCI modeling (section 4.2) of the spectra in Figures 1 and 2.

#### 4.1.1. Geometric Structures

Calculations were performed starting from the crystal structure of low-spin ( $S = 0$ ) ferrous  $[\text{Fe}^{\text{II}}(\text{pfp})(1\text{-MeIm})_2]$ .<sup>7,56</sup> Geometry optimization did not appreciably alter the geometric or electronic structure of this complex ([Table 2]). Geometry optimized models for low-spin ( $S = 0$ ) ferrous  $[\text{Fe}^{\text{II}}(\text{pfp})(1\text{-MeIm})(\text{CO})]$ , low-spin ferric ( $S = 1/2$ )  $[\text{Fe}^{\text{III}}(\text{pfp})(1\text{-MeIm})_2]^+$  and intermediate-spin ( $S = 1$ )  $[\text{Fe}^{\text{II}}(\text{pfp})]$  were generated from the crystal structure of  $[\text{Fe}^{\text{II}}(\text{pfp})(1\text{-MeIm})_2]$  by exchanging the axial 1-MeIm ligand with CO or by removing both axial ligands generating a 4-coordinate complex. For reference, first shell optimized bond lengths of  $[\text{Fe}^{\text{II}}(\text{tpp})(\text{ImH})_2]$  and  $[\text{Fe}^{\text{III}}(\text{tpp})(\text{ImH})_2]^+$  are also provided in Table 2, and SI Figure S5 shows a comparison with previous results and to describe any difference between heme bonding in the picket fence porphyrin (pfp) and tetraphenyl porphyrin (tpp).<sup>36</sup>

The first shell bond lengths of all optimized structures along with crystallographic distances are given in Table 2. In tpp, the creation of the  $d\pi$  hole in the ferric complex results in

increased donation from the heme ring<sup>36</sup> and a slight elongation (0.01 Å) in the Fe-equatorial and axial Fe–imidazole bonds. However, in pfp, the steric bulk of the pickets results in asymmetric axial bond lengths, with the longer bond in the sterically constrained picket cage. In addition, the steric interactions of the pickets causes a slight ruffling of the heme in pfp, relative to tpp which is planar, and can be seen in the out-of-plane distances for the iron atom. Exchanging the axial 1-MeIm for a carbonyl group results in the largest structural change of any pfp complex with a short 1.73 Å axial Fe–CO bond. This short bond results in a significant trans-effect with a long 2.06 Å axial Fe–imidazole bond. The short CO bond also produces longer equatorial bonds due to the weaker Fe–heme interactions with the donut of the  $d_z^2$  orbital. The opposite occurs for the 4-coordinate complex, which exhibits the shortest equatorial bonds of any pfp complex at an average of 1.98 Å (Table 2).

#### 4.1.2. Electronic Structures

[Figure 3] shows the energy levels, orbital contours, and the decomposition of the orbital fragments from a Mulliken population analysis of  $[\text{Fe}^{\text{II}}(\text{pfp})(1\text{-MeIm})_2]$ ,  $[\text{Fe}^{\text{II}}(\text{pfp})(1\text{-MeIm})(\text{CO})]$ ,  $[\text{Fe}^{\text{III}}(\text{pfp})(1\text{-MeIm})_2]^+$ , and  $[\text{Fe}^{\text{II}}(\text{pfp})]$  from left to right respectively with those of  $[\text{Fe}^{\text{II}}(\text{tpp})(\text{ImH})_2]$  and  $[\text{Fe}^{\text{III}}(\text{tpp})(\text{ImH})_2]^+$  given in SI Figure S5.

The molecular orbital diagram of  $[\text{Fe}^{\text{II}}(\text{pfp})(1\text{-MeIm})_2]$  is very similar to that reported for  $[\text{Fe}^{\text{II}}(\text{tpp})(\text{ImH})_2]$ <sup>36</sup> with two main sets of Fe d-orbitals, the unoccupied  $b_{1g} d_{x^2-y^2}$  {335} and  $a_{1g} d_z^2$  {329} (referenced to  $D_{4h}$  symmetry), with the occupied  $e_g d_{xz}$  {323},  $d_{yz}$  {324}, and  $b_{2g} d_{xy}$  {325} lower in energy (Figure 3, left). In between these sets of 3d orbitals are the approximately degenerate low-lying unoccupied porphyrin  $\pi^*$  orbitals {326 and 327} which contain some (10%) iron  $d_{xz}$  and  $d_{xy}$  character, due to backbonding. Similar to tpp,<sup>36</sup> the  $d_{x^2-y^2}$  molecular orbital is highest in energy indicating that the porphyrin is a stronger  $\sigma$ -donor relative to 1-MeIm. However, there is a greater amount of metal character in both the  $d_{x^2-y^2}$  and the  $d_z^2$  orbital, 68% vs. 66% and 69% vs. 66% respectively for pfp relative to tpp (SI Figure S5). This indicates that the  $\sigma$ -donation into the  $d_{x^2-y^2}$  and  $d_z^2$  orbitals from the heme and imidazole in the pfp complex(s) is not as strong as in tpp, consistent with the heme ruffling and the longer axial bonds described above.

In  $[\text{Fe}^{\text{II}}(\text{pfp})(1\text{-MeIm})(\text{CO})]$ , the carbonyl is a stronger field ligand compared to 1-MeIm. As suggested by its short 1.73 Å Fe–CO bond, the strong  $\sigma$ -donation of the CO lone pair

destabilizes the  $d_z^2$  orbital {315} to higher energy relative to the other d orbitals (Figure 3). This shift is accompanied by a decrease in metal character in the  $d_z^2$  orbital from 69% to 57% for  $[\text{Fe}^{\text{II}}(\text{pfp})(1\text{-MeIm})(\text{CO})]$  relative to  $[\text{Fe}^{\text{II}}(\text{pfp})(1\text{-MeIm})_2]$ . The CO also adds an additional set of low-lying CO  $\pi^*$  orbitals {325 and 326} above the 3d  $\sigma$  orbitals. These CO  $\pi^*$  orbitals contain some metal d-character from the  $d_{xz}$  {307} and  $d_{yz}$  {308} orbitals, calculated at  $\sim 15\%$ . The backbonding into the CO  $\pi^*$  orbitals decreases the amount of backbonding into the porphyrin  $\pi^*$  orbitals {311 and 312} which now contain only half ( $\sim 5\%$ ) the metal character compared to those of  $[\text{Fe}^{\text{II}}(\text{pfp})(1\text{-MeIm})_2]$ . Thus, CO is a stronger backbonding ligand than the porphyrin. While not directly impacting the L-edge, the calculations show that this increase in backbonding also stabilizes the  $d_{xz/yz}$  set, resulting in a larger splitting between the occupied  $d_{xz/yz}$  and  $d_{xy}$  orbitals (Figure 3). However, the L-edge transitions into the CO  $\pi^*$  orbitals can be directly observed in the spectrum as the intense high-energy peak on the  $L_3$ - and  $L_2$ -edge at 710.0 and 722.6 eV respectively (*vide infra*), Figure 2A.

For the low-spin ( $S = 1/2$ ) ferric complex  $[\text{Fe}^{\text{III}}(\text{pfp})(1\text{-MeIm})_2]^+$ , the additional hole in the  $d_{xz}$  orbital allows  $\pi$ -donation from the occupied porphyrin  $\pi$  orbitals into the  $d\pi$ -hole reducing the calculated metal d-character in the  $d_{xz}$  orbital {325} from 70% to 67% relative to  $[\text{Fe}^{\text{II}}(\text{pfp})(1\text{-MeIm})_2]$  (Figure 3). This also results in a decrease in backbonding into the porphyrin  $\pi^*$  orbitals, from 10% to 6% {326 and 327} for  $[\text{Fe}^{\text{II}}(\text{pfp})(1\text{-MeIm})_2]$  to  $[\text{Fe}^{\text{III}}(\text{pfp})(1\text{-MeIm})_2]^+$  respectively. This is similar to that observed for  $[\text{Fe}^{\text{III}}(\text{tpp})(\text{ImH})_2]^+$  relative to  $[\text{Fe}^{\text{II}}(\text{tpp})(\text{ImH})_2]^+$  (SI Figure S5).<sup>36</sup> Additionally, the longer axial bond in  $[\text{Fe}^{\text{III}}(\text{pfp})(1\text{-MeIm})_2]^+$  (Table 2) stabilizes the  $d_z^2$  orbital, and results in a  $\sim 0.5$  eV increase in energy splitting between  $d_z^2$  {328} and  $d_{x^2-y^2}$  {329} orbital for both the  $\alpha$  and  $\beta$  spins, as compared to  $[\text{Fe}^{\text{II}}(\text{pfp})(1\text{-MeIm})_2]$ , despite the  $\sim 3\%$  increase in covalency in the  $d_z^2$  orbital.

In  $[\text{Fe}^{\text{II}}(\text{pfp})]$ , the lack of axial ligands results in a large stabilization of the  $d_z^2$  orbital and an intermediate-spin  $S = 1$  ground state with two  $\alpha$  electrons and two  $\beta$  holes in the  $d_z^2$  and  $d_{xz}$  orbitals (Figure 3, right and SI Figure S6). The occupied  $\alpha$   $d_z^2$  orbital {265} has been shifted below the HOMO/LUMO gap, and with no axial ligands the amount of metal character in the  $d_z^2$  orbital has increased from 69% to 83% in  $[\text{Fe}^{\text{II}}(\text{pfp})]$  relative to  $[\text{Fe}^{\text{II}}(\text{pfp})(1\text{-MeIm})_2]$  (Figure 3, right). The presence of the  $\beta$  hole in the  $d_{xz}$  also allows for  $\pi$ -donation from the heme, resulting in an average of 83% metal character in the  $d_{xz/yz}$  orbitals (SI Figure S6), and a decrease in  $\pi$ -backbonding to  $\sim 4\%$  { $\alpha$  283 and 284}, similar to that found for the low-spin ferric heme complexes.<sup>36</sup>

## 4.2. VBCI Modeling of Reference Complexes

Based on the above DFT calculations which indicate only small differences in the heme bonding interactions between tpp and pfp, the iron L-edge of  $[\text{Fe}^{\text{II}}(\text{pfp})(1\text{-MeIm})_2]$  was simulated starting from the previous fit to  $[\text{Fe}^{\text{II}}(\text{tpp})(\text{ImH})_2]$ .<sup>36</sup> VBCI fitting was done using an iterative approach by first taking into account ligand field effects followed by covalency contributions, maintaining the same  $T$ ,  $\Delta$ , and  $\Delta_{\text{BB}}$  parameters for the ground and final states. The final multiplet fit to  $[\text{Fe}^{\text{II}}(\text{pfp})(1\text{-MeIm})_2]$  is presented in [Figure 4] with fit parameters given in [Table 3]. For reference, VBCI fits to the uncorrected L-edge data are also given in SI Figure S7. This fit yielded projected differential orbital covalencies (DOC) of 68%, 69%, and 8%, metal character in the unoccupied  $d_{x^2-y^2}$ ,  $d_z^2$ , and the porphyrin  $\pi^*$  orbitals respectively [Table 4]; results consistent with the DFT calculations presented in Figure 3. The multiplet fit to the L-edge spectrum of  $[\text{Fe}^{\text{II}}(\text{pfp})(1\text{-MeIm})_2]$  was used as a reference for fitting the remaining complexes.

There are four differences in the L-edge spectrum of  $[\text{Fe}^{\text{II}}(\text{pfp})(1\text{-MeIm})(\text{CO})]$  relative to that of  $[\text{Fe}^{\text{II}}(\text{pfp})(1\text{-MeIm})_2]$  (Figure 2A). The first is a sharpening of the  $L_3$ -edge which was simulated by an increase in the energy of the  $d_z^2$  orbital by a decrease in  $Dt$  and by an increase in the  $\sigma$ -LMCT mixing through  $T$  ( $a_{1g}$ ). These changes reflect the strong  $\sigma$ -donation of the CO. The second is the additional high-energy feature at 710.0 eV (Figure 2A) which was accounted for by an increase in the amount of MLCT from the occupied iron  $d\pi$  into the CO  $\pi^*$  orbitals ([Figure 5]). The last differences are an increase in total intensity and a shift of the spectrum to higher energy. These reflect an increase in the ligand field and the unoccupied d-character in the valence orbitals (effective number of holes) due to the additional backbonding. The final fit of  $[\text{Fe}^{\text{II}}(\text{pfp})(1\text{-MeIm})(\text{CO})]$  yields 64% metal character in  $b_{1g}$ , 60% in  $a_{1g}$ , and 20% in the  $\pi^*$  orbital set, with the last value reflecting contributions to both the porphyrin and the CO  $\pi^*$  orbitals. Based on the DFT calculation of  $[\text{Fe}^{\text{II}}(\text{pfp})(1\text{-MeIm})(\text{CO})]$ , Figure 3, these two contributions can be separated with  $\sim 5\%$  porphyrin and  $\sim 15\%$  CO  $\pi^*$  backbonding from the iron  $d_{xz/yz}$  orbital set. A final fit is presented in [Figure 6], with fit parameters, projected orbital covalencies, and comparisons to DFT calculations, in Tables 3 and 4 respectively.

The dominant spectroscopic differences between the 6-coordinate low-spin ( $S = 0$ )  $[\text{Fe}^{\text{II}}(\text{pfp})(1\text{-MeIm})_2]$  and the 4-coordinate intermediate-spin ( $S = 1$ )  $[\text{Fe}^{\text{II}}(\text{pfp})]$  complex are the much broader  $L_3$ -edge and the unique spectral shape with three well defined features (Figure

2C). Starting from  $[\text{Fe}^{\text{II}}(\text{pfp})(1\text{-MeIm})_2]$ , these spectral changes were simulated by adjusting the ligand field parameters  $10Dq$ ,  $Ds$ , and  $Dt$  to stabilize the  $d_z^2$  orbital relative to the d-manifold ([Figure 7]). This results in a discontinuity in the L-edge progression where the ground state changes from a low-spin  $S = 0$  to an intermediate-spin  $S = 1$  once the  $d_z^2$  orbital is low enough in energy to depopulate one  $d\pi$  electron from the filled subshell of the  $S = 0$   $[\text{Fe}^{\text{II}}(\text{pfp})(1\text{-MeIm})_2]$  complex. This spin state change results in the spectral broadening and the three-peak multiplet structure observed in the L-edge spectrum. To generate a final VBCI fit for the 4-coordinate  $[\text{Fe}^{\text{II}}(\text{pfp})]$  complex, [Figure 8], LMCT and MLCT parameters were adjusted to decrease  $\sigma$ -donation into the  $a_{1g}$ , and  $\pi$ -backbonding into the porphyrin  $\pi^*$  orbitals, relative to  $[\text{Fe}^{\text{II}}(\text{pfp})(1\text{-MeIm})_2]$ , Table 3. This produced an increase in metal character from 69% to 85% in the  $d_z^2$  orbital (Table 4), as observed in the DFT calculations, and reflects the loss of the axial ligands.

The higher resolution L-edge data of low-spin ferric ( $S = 1/2$ )  $[\text{Fe}^{\text{III}}(\text{tpp})(\text{ImH})_2]\text{Cl}$ , Figure 2D, were refit as described above using the same  $T$ ,  $\Delta$ , and  $\Delta_{\text{BB}}$  parameters for the ground and final states relative to reference 36 ([Figure 9]). The resulting fit parameters, Table 3, reproduce the previous study,<sup>36</sup> where the presence of the  $d\pi$  hole allows for 17%  $\pi$ -donation from the heme and decreases the amount of MLCT backbonding into the porphyrin  $\pi^*$  orbitals from 8% to 4% relative to  $[\text{Fe}^{\text{II}}(\text{pfp})(1\text{-MeIm})_2]$ .

#### 4.3.1. Oxy-PFP: VBCI Modeling of L-edge XAS

To quantitatively analyze the L-edge spectrum of oxy-picket fence porphyrin,  $[\text{Fe}(\text{pfp})(1\text{-MeIm})\text{O}_2]$  Figure 2B, two series of systematic simulations were evaluated starting from both the ferrous and ferric limits of the VBCI model ([Figure 10]). From the fit parameters of  $[\text{Fe}^{\text{II}}(\text{pfp})(1\text{-MeIm})_2]$ , Table 3, the energy of the MLCT  $d^{N-1}$  configuration,  $\pi^* \Delta_{\text{BB}}$ , was systematically decreased from  $-1.65$  to  $-8.65$  eV in steps of 0.64 eV. The fit of  $[\text{Fe}^{\text{II}}(\text{pfp})(1\text{-MeIm})_2]$  (the low-spin  $d^6$  reference), is given by the first trace, A, in Figure 10, left. Note, this simulation differs from that in Figure 4 due to an increase in the ligand field required to maintain the low-spin configuration throughout this series (i.e. the spin paring energy is higher for a ferric relative to a ferrous complex, SI Figure S8). Throughout the progression, each trace was projected and the amount of backbonding quantified in terms of its  $d\pi^*$  character.

As the backbonding is increased (i.e the energy of  $\Delta_{\text{BB}}$  is decreased and becomes dominant), the ratio of the  $d^N$  ( $d^6$ ) relative to the  $d^{N-1}L^-$  ( $d^5$ ) configuration changes and more charge is transferred from the iron  $d\pi$  orbitals to the  $\text{O}_2$  through MLCT mixing. Between  $\Delta_{\text{BB}}$  of

–4.20 and –4.83 eV the  $d^{N-1}$  configuration becomes dominant, trace B, and the  $d\pi$  hole starts to appear in the lower energy region of the simulated spectrum (\*). This feature in the iron L-edge is characteristic of a low-spin ferric contribution, where the intensity in this peak is proportional to the amount of  $\pi$ -backbonding into  $O_2$  from the iron  $d\pi$  orbitals. At a  $\Delta_{BB}$  of –6.74 eV, trace C, the amount of  $d\pi^*$  character is 84%, similar to the amount of  $d\pi$  hole character in the low-spin ferric heme reference  $[Fe^{III}(tpp)(ImH)_2]Cl$ , Figure 9 and Table 4. As  $\Delta_{BB}$  is further decreased, the simulation approaches a pure low-spin  $d^5$  state, with the final trace, D, at 90%  $d\pi^*$  hole at a  $\Delta_{BB}$  of –8.65 eV.

Starting from the final fit parameters of  $[Fe^{III}(tpp)(ImH)_2]Cl$  as a low-spin ferric  $d^5$  reference, trace D' in Figure 10 right, the reverse trend is generated by systematically increasing the  $O_2^-$   $\pi$ -donation (i.e. decreasing  $\Delta$  from –0.6 to –9.4 eV). Over this progression of simulations the amount of  $d\pi$  hole character (peak marked with \* on the low-energy side of the  $L_3$ -edge) decreases as the amount of LMCT from the  $O_2^-$  to the iron  $d\pi$  hole is increased. At a  $\Delta$  of –2.20 eV the amount of  $\pi$ -bonding gives a similar  $d\pi$  hole character as that found for  $[Fe^{III}(tpp)(ImH)_2]Cl$ , trace C'. As with the progression from  $d^6$  to  $d^5$  (Figure 10 left), a simulated spectrum is reached at a  $\Delta \approx -4.60$  eV where the  $d^6$  configuration starts to become the main component of the wavefunction, trace B', and the  $d\pi$  hole spectral feature is no longer clearly distinguishable. At the end of the series ( $\Delta = -7.80$  eV) the wavefunction contains only ~10%  $d\pi$  hole character and the simulated spectral shape looks very similar to the iron L-edge spectrum of  $[Fe^{II}(pfp)(1-MeIm)_2]$ , trace A' and Figure 4.

Note, the VBCI simulation of the  $d^6$  spectrum from a  $d^5$  starting point has some differences from the fit presented in Figure 4 as this simulation lacks the  $d^{N+1}$  ( $d^7$ ) contribution and contains some  $d^{N-1}$  ( $d^4$ ) configuration. Likewise, the  $d^6$  simulation of the  $d^5$   $[Fe^{III}(tpp)(ImH)_2]Cl$  lacks  $d^{N-1}$  ( $d^4$ ) and contains some  $d^{N+1}$  ( $d^7$ ) configuration. However, both simulations do contain the dominant,  $d^5$  and  $d^6$ , contributions to the multiplet spectrum, making the above interconversions reasonable.

Using this approach, these simulations can estimate the amount of  $d\pi^*$  character in  $[Fe(pfp)(1-MeIm)O_2]$  as the spectral shape of  $[Fe(pfp)(1-MeIm)O_2]$  (Figure 2B) lacks the characteristic low-energy  $d\pi$  hole feature common to low-spin ferric species (Figure 2D). Starting from the  $d^6$  limit (Figure 10, left), increasing the amount of backbonding (MLCT) in the simulations from the  $d\pi$  into  $O_2$  gives an upper limit of 30%  $d\pi^*$  character at a  $\Delta_{BB} = -3.56$  eV, trace O. A similar limit is determined starting from the  $d^5$  configuration by increasing the

amount  $\pi$  donation (LMCT) from the  $O_2^-$  into the iron  $d\pi$  orbital. This again gives an upper limit of 30% at a  $\Delta$  of  $-5.40$  eV, trace  $O'$ . These two sets of traces define  $[Fe(pfp)(1-MeIm)O_2]$  as having most of the  $\pi$  electron density at the iron, with an upper limit of 30%  $d\pi$  hole character in the ground state.

A final fit to the L-edge spectrum of  $[Fe(pfp)(1-MeIm)O_2]$  was obtained using a  $d^6$  ground state configuration with MLCT ( $d^5$ ) and LMCT ( $d^7$ ) configuration interaction ([Figure 11]). Projection of the fit yields values of 67%, 64%, and 11% metal d-character in the  $d_{x^2-y^2}$ ,  $d_z^2$  and  $d\pi^*$  orbitals respectively, [Table 5], with fit parameters given in Table 3. This electronic structure description of  $[Fe(pfp)(1-MeIm)O_2]$  has the  $d_{x^2-y^2}$  molecular orbital highest in energy due to the strong  $\sigma$ -donation from the heme, followed by the  $d_z^2$  orbital with strong  $\sigma$ -donation from dioxygen. A range of final fits to the data, SI Figure S9, gave up to 15% metal character in the low-energy  $d\pi$  hole. This combined with the simulations in Figure 10, and the VBCI multiplet fits of  $[Fe^{II}(pfp)(1-MeIm)_2]$  and  $[Fe^{III}(tpp)(ImH)_2]^+$ , which quantified the relative amounts of  $d\pi$  hole character in each reference complex at 8% and 83% respectively (Figures 4, 9, S10 and Table 4), the  $d\pi$  hole character in  $[Fe(pfp)(1-MeIm)O_2]$  is  $15 \pm 5\%$ ; describing  $[Fe(pfp)(1-MeIm)O_2]$  as having most of the  $d\pi$  electron density on the iron.

#### 4.3.2. Oxy-PFP: DFT of Calculations

To compare with the literature calculations of the Fe– $O_2$  bond in heme proteins,<sup>10,22,24-26</sup> DFT calculations were performed on  $[Fe(pfp)(1-MeIm)O_2]$  (SI Figure S11). Geometry optimization of  $[Fe(pfp)(1-MeIm)O_2]$  did not appreciably change the structure from that of the crystal structure<sup>57,65</sup> and gave first shell bond lengths and angles similar to those found in oxy-heme proteins (SI Table S1).<sup>66,67</sup>

These calculations gave both spin unpolarized, and spin polarized results, with the latter – 2.4 kcal/mol lower in energy (SI Table S2). Both calculations gave comparable amounts of total metal character in the unoccupied valence orbitals and an appreciable amount of negative charge localized on the  $O_2$  of  $[Fe(pfp)(1-MeIm)O_2]$ , similar to values recently reported for DFT/MM calculations of oxy-myoglobin (SI Table S2).<sup>10</sup> Mulliken population analysis of the polarized calculation yielded 65/64% and 62/57% metal character for the  $d_{x^2-y^2}$  {316} and  $d_z^2$  {315}  $\alpha/\beta$  spin orbitals respectively and an average of  $\sim 6\%$  metal character in the porphyrin  $\pi^*$  orbitals {313-314}, Table 5. These values compared well to the VBCI fit to the L-edge data. Additionally, the lower energy calculation showed spin polarization of the  $d\pi$  electron density

with orbital {312} containing 57%  $d_{xz}$  character in the  $\alpha$  manifold and 11% in the  $\beta$  (SI Figure S11). This large degree of spin polarization is not consistent with the absence of the low-energy  $d\pi$  hole observed in the L-edge spectrum of  $[\text{Fe}(\text{pfp})(1\text{-MeIm})\text{O}_2]$  (Figure 2B), a feature characteristic of a low-spin ferric complex (Figure 2D).

## 5. Discussion

An array of spectroscopic and computational methods have been applied to evaluate the nature of the Fe–O<sub>2</sub> bond in oxy-hemoglobin and oxy-myoglobin.<sup>10,17-26</sup> In this study, iron L-edge X-ray absorption spectroscopy has been used to experimentally probe the electronic structure description of the Fe–O<sub>2</sub> center in  $[\text{Fe}(\text{pfp})(1\text{-MeIm})\text{O}_2]$ .<sup>7,8</sup>

Three model complexes provide well defined references: the low-spin ( $S = 0$ ) ferrous complex,  $[\text{Fe}^{\text{II}}(\text{pfp})(1\text{-MeIm})_2]$ , as in the Pauling description for the iron;<sup>6,11</sup> the low-spin ( $S = 1/2$ ) ferric complex  $[\text{Fe}^{\text{III}}(\text{tpp})(\text{ImH})_2]\text{Cl}$  as in the Weiss model;<sup>12</sup> and an intermediate-spin ( $S = 1$ ) ferrous,  $[\text{Fe}^{\text{II}}(\text{pfp})]$  complex with one unpaired electron in the  $d_z^2$  and one in the  $d_{xz}$  orbital as in the McClure-Goddard-Harcourt Ozone model.<sup>13-16</sup> To facilitate this discussion, an overlay of the L-edge data of the three reference models with that of  $[\text{Fe}(\text{pfp})(1\text{-MeIm})\text{O}_2]$  is presented in [Figure 12]. From this overlay, the L-edge spectrum of  $[\text{Fe}(\text{pfp})(1\text{-MeIm})\text{O}_2]$  is most similar to that of low-spin ferrous  $[\text{Fe}^{\text{II}}(\text{pfp})(1\text{-MeIm})_2]$ . However, it does exhibit some differences in multiplet structure such as a sharpening of the main L<sub>3</sub> feature and additional intensity on the high-energy side. This indicates that the electronic structure of the iron in the Fe–O<sub>2</sub> center is not simply described by any of these models. Of the three references, the iron L-edge of  $[\text{Fe}^{\text{II}}(\text{pfp})]$  has the least resemblance to that of  $[\text{Fe}(\text{pfp})(1\text{-MeIm})\text{O}_2]$ , as it exhibits a very different multiplet structure in both the L<sub>3</sub>- and L<sub>2</sub>-edge as well as a slight shift of 0.1 eV to lower energy, relative to  $[\text{Fe}^{\text{II}}(\text{pfp})(1\text{-MeIm})_2]$ . Compared to the low-spin ferric  $[\text{Fe}^{\text{III}}(\text{tpp})(\text{ImH})_2]\text{Cl}$  complex, the L-edge spectrum of  $[\text{Fe}(\text{pfp})(1\text{-MeIm})\text{O}_2]$  is also significantly different as it does not exhibit the signature low-energy peak associated with the  $d\pi$  hole.

Analysis of the L-edge data on  $[\text{Fe}(\text{pfp})(1\text{-MeIm})\text{O}_2]$  (Figure 12) also shows a strong  $\sigma$ -donation from the O<sub>2</sub> into the  $d_z^2$  orbital of the iron. This leads to a sharpening of the dominant feature in the L<sub>3</sub>-edge relative to  $[\text{Fe}^{\text{II}}(\text{pfp})(1\text{-MeIm})_2]$  (Figure 2B). This  $\sigma$ -donation, together with the strong  $\pi$ -interaction affects the  $Z_{\text{eff}}$  of the iron in the Fe–O<sub>2</sub> complex. This is measured experimentally by the total d-character in the unoccupied valence orbitals and by the energy

position of the L<sub>3</sub>-edge. In going from [Fe<sup>II</sup>(pfp)(1-MeIm)<sub>2</sub>] to [Fe<sup>II</sup>(pfp)(1-MeIm)(CO)] to [Fe<sup>III</sup>(tpp)(ImH)<sub>2</sub>]Cl the energy of the L<sub>3</sub>-edge and the intensity of the spectra increase from 708.2/38, to 708.6/41, to 709.2/46, eV/normalized units respectively, Table 1, reflecting the increase in Z<sub>eff</sub>. These same values for the L-edge of [Fe(pfp)(1-MeIm)O<sub>2</sub>] are 708.3 eV and 39 normalized units indicating a Z<sub>eff</sub> higher than that of [Fe<sup>II</sup>(pfp)(1-MeIm)<sub>2</sub>], but significantly lower than that of the [Fe<sup>III</sup>(tpp)(ImH)<sub>2</sub>]Cl complex.

From the VBCI simulations in Figure 10, starting from a low-spin ferrous limit (left side), the dπ hole in the L-edge simulation appears as the MLCT backbonding from the iron into the π\* orbital of O<sub>2</sub> is increased. At ≥ 30% dπ hole character in the ground state, the low-energy feature is clearly present. Alternatively, starting from the low-spin ferric limit that possesses a prominent low-energy dπ feature in the simulated L-edge spectrum, increasing the amount of LMCT from the occupied π\* orbital of O<sub>2</sub><sup>-</sup> into the unoccupied dπ orbital on the iron increases the energy and decreases the intensity of this low-energy feature. With a large π-donation corresponding to ≤ 30% dπ hole character remaining in the ground state, the low-energy feature in the simulated spectrum is again no longer present, as in the iron L-edge spectrum of [Fe<sup>II</sup>(pfp)(1-MeIm)<sub>2</sub>]. Thus, if one starts from a Fe<sup>III</sup>-O<sub>2</sub><sup>-</sup> bonding description, the L-edge data of [Fe(pfp)(1-MeIm)O<sub>2</sub>] clearly demonstrate the presence of a strong O<sub>2</sub><sup>-</sup> π-donor interaction with the iron dπ orbital. As presented by Shaik,<sup>10</sup> the stronger the π-bonding interaction between the iron and O<sub>2</sub>, the less spin polarization is likely to be present for the π electrons. A strong spin polarization, however, corresponds to an antiferromagnetically coupled description of the bond between the O<sub>2</sub> and the heme iron. Note that in picket fence porphyrin, there is no hydrogen bond to the distal oxygen of the Fe-O<sub>2</sub> site. From QM/MM calculations, this hydrogen bond is expected to play an important role in this spin polarization.<sup>10</sup> Thus, it will be important to compare these L-edge data and results to parallel data on oxy-hemoglobin and oxy-myoglobin.

## 6. Summary

Most spectroscopic studies of dioxygen bonding in heme systems have been complicated by the highly delocalized nature of the porphyrin, and calculations have required analysis of a multi-determinant description of the highly covalent Fe-O<sub>2</sub> bond.<sup>17-26</sup> Here, we have shown that the iron L-edge XAS provides a direct probe of the iron center in this highly covalent environment. The L-edge data of the dioxygen bond in the heme complex [Fe(pfp)(1-MeIm)O<sub>2</sub>] do not exhibit the low-energy feature of a hole in the dπ orbital of the iron, as is characteristic of

all low-spin ferric complexes.<sup>36-38</sup> The absence of this feature requires a strong  $\pi$ -interaction between the iron and the O<sub>2</sub> that will limit the extent of spin polarization in the Fe–O<sub>2</sub> bond. Parallel studies are now underway to probe this bonding interaction in the protein environment of oxy-hemoglobin and oxy-myoglobin, which requires that the data be obtained using resonant inelastic X-ray scattering (RIXS).

## ***Associated Content***

### **Supporting Information**

Additional tables, figures, multiplet fits, computational results, and optimized structural coordinates are included along with the entire reference 58 in the supporting information. This material is available free of charge via the Internet at <http://pubs.acs.org>.

## ***Author Information***

### **Corresponding Author**

hedman@slac.stanford.edu; hodgson@slac.stanford.edu; and edward.solomon@stanford.edu

### **Present Addresses**

<sup>A</sup>R.A.D. Department of Chemistry, Université de Bourgogne, Institut de Chimie Moléculaire, 9 Av. Alain Savary, Sciences Mirande, 21078 Dijon, France.

<sup>B</sup>R.K.H. School of Chemistry and Monash Centre for Synchrotron Science, Clayton, Australia, 3800

<sup>C</sup>M.L. Department of Chemistry, Ångström laboratory, Uppsala University, Box 518, SE-751 20 Uppsala, Sweden

### **Notes**

The authors declare no competing financial interest.

## ***Acknowledgements***

This work was supported by National Institutes of Health (NIH) grants GM 40392 (E.I.S.), 5P41RR-001209-32, and 8P41GM 103393-33 (K.O.H.), and by the National Science Foundation (NSF) grant MCB 0919027 (E.I.S.). Portions of this research were carried out at the Stanford Synchrotron Radiation Lightsource (SSRL), a Directorate of SLAC National Accelerator Laboratory and an Office of Science User Facility operated for the U.S. Department of Energy (DOE) Office of Science by Stanford University. The SSRL Structural Molecular Biology Program is supported by the DOE Office of Biological and Environmental Research and by the NIH, National Institute of General Medical Sciences (NIGMS) (including P41GM103393) and the National Center for Research Resources (NCRR) (P41RR001209).

R.A.D. was supported by NIH GM-069658 to James P. Collman. T.K. thanks the German Research Foundation (DFG) grant KR3611/2. R.K.H. thanks the Monash Centre for Synchrotron Science for a Fellowship. M.L. thanks the Marcus and Amalia Wallenberg foundation for financial support.

## ***Abbreviations***

X-ray Absorption Spectroscopy (XAS), Oxy-hemoglobin (Hb), Oxy-myoglobin (Mb), Picket Fence Porphyrin (pfp), Ligand to Metal Charge Transfer (LMCT), Metal to Ligand Charge Transfer (MLCT), Configuration Interaction (CI), Differential Orbital Covalency (DOC).

## References and Notes

- (1) Springer, B. A.; Sligar, S. G.; Olson, J. S.; Phillips, G. N., Jr. *Chem. Rev.* **1994**, *94*, 699-714.
- (2) Dickerson, R. E.; Geiss, I. *Hemoglobin: Structure, Function, Evolution, and Pathology*; Benjamin/Cummings: Menlo Park, CA, 1983.
- (3) Shikama, K. *Chem. Rev.* **1998**, *98*, 1357-1373.
- (4) Perutz, M. F.; Fermi, G.; Luisi, B.; Shaanan, B.; Liddington, R. C. *Acc. Chem. Res.* **1987**, *20*, 309-321.
- (5) Gamgee, A. *Proc. R. Soc. Lond.* **1901**, *68*, 503-512.
- (6) Pauling, L.; Coryell, C. D. *Proc. Natl. Acad. Sci. U.S.A.* **1936**, *22*, 210-216.
- (7) Collman, J. P.; Gagne, R. R.; Reed, C. A.; Halbert, T. R.; Lang, G.; Robinson, W. T. *J. Am. Chem. Soc.* **1975**, *97*, 1427-1439.
- (8) Collman, J. P.; Brauman, J. I.; Halbert, T. R.; Suslick, K. S. *Proc. Natl. Acad. Sci. U.S.A.* **1976**, *73*, 3333-3337.
- (9) Shaanan, B. *J. Mol. Biol.* **1983**, *171*, 31-59.
- (10) Chen, H.; Ikeda-Saito, M.; Shaik, S. *J. Am. Chem. Soc.* **2008**, *130*, 14778-14790.
- (11) Pauling, L. *Nature* **1964**, *203*, 182-183.
- (12) Weiss, J. J. *Nature* **1964**, *202*, 83-84.
- (13) Mclure, D. S. *Radiation. Res. Suppl.* **1960**, *2*, 218.
- (14) Harcourt, R. D. *Int. J. Quantum Chem.* **1971**, *5*, 479-495.
- (15) Harcourt, R. D. *Chem. Phys. Lett.* **1990**, *167*, 374-377.
- (16) Goddard, W. A.; Olafson, B. D. *Proc. Natl. Acad. Sci. U.S.A.* **1975**, *72*, 2335-2339.
- (17) Spiro, T. G.; Strekas, T. C. *J. Am. Chem. Soc.* **1974**, *96*, 338-345.
- (18) Yamamoto, T.; Palmer, G.; Gill, D.; Salmeen, I. T.; Rimai, L. *J. Biol. Chem.* **1973**, *248*, 5211-5213.
- (19) Marchant, L.; Sharrock, M.; Hoffman, B. M.; Münck, E. *Proc. Natl. Acad. Sci.* **1972**, *69*, 2396-2399.
- (20) Champion, P. M.; Collins, D. W.; Fitchen, D. B. *J. Am. Chem. Soc.* **1976**, *98*, 7114-7115.
- (21) Morikis, D.; Sage, J. T.; Rizos, A. K.; Champion, P. M. *J. Am. Chem. Soc.* **1988**, *110*, 6341-6342.
- (22) Jensen, K. P. *J. Inorg. Biochem.* **2005**, *99*, 45-54.
- (23) Jensen, K. P.; Bell, C. B. I.; Clay, M. D.; Solomon, E. I. *J. Am. Chem. Soc.* **2009**, *131*, 12155-12171.
- (24) Jensen, K. P.; Roos, B. O.; Ryde, U. *J. Inorg. Biochem.* **2005**, *99*, 978.
- (25) Jensen, K. P.; Ryde, U. *J. Biol. Chem.* **2004**, *279*, 14561-14569.
- (26) Ribas-Ariño, J.; Novoa, J. J. *Chem. Commun.* **2007**, 3160-3162.
- (27) Barlow, C. H.; Maxwell, J. C.; Wallace, W. J.; Caughey, W. S. *Biochem. Biophys. Res. Commun.* **1973**, *55*, 91-95.
- (28) Spartalian, K.; Lang, G.; Yonetani, T. *Biochim Biophys Acta* **1976**, *428*, 281-290.
- (29) Reynolds, C. H. *J. Org. Chem.* **1988**, *53*, 6061-6064.
- (30) Yamamoto, U.; Noro, T.; Ohno, K. *Int. J. Quantum Chem.* **1992**, *42*, 1563-1575.
- (31) Ghosh, A. *J. Phys. Chem. B* **1997**, *101*, 3290-3297.
- (32) Lamoen, D.; Parrinello, M. *Chem. Phys. Lett.* **1996**, *248*, 309-315.
- (33) Matsuzawa, N.; Ata, M.; Dixon, D. A. *J. Phys. Chem.* **1995**, *99*, 7698-7706.
- (34) Loew, G. H.; Harris, D. L. *Chem. Rev.* **2000**, *100*, 407-419.
- (35) Sono, M.; Roach, M. P.; Coulter, E. D.; Dawson, J. H. *Chem. Rev.* **1996**, *96*, 2841-2888.
- (36) Hocking, R. K.; Wasinger, E. C.; Yan, Y.-L.; de Groot, F. M. F.; Walker, F. A.; Hodgson, K. O.; Hedman, B.; Solomon, E. I. *J. Am. Chem. Soc.* **2007**, *129*, 113-125.
- (37) Wasinger, E. C.; de Groot, F. M. F.; Hedman, B.; Hodgson, K. O.; Solomon, E. I. *J. Am. Chem. Soc.* **2003**, *125*, 12894-12906.
- (38) Hocking, R. K.; Wasinger, E. C.; de Groot, F. M. F.; Hodgson, K. O.; Hedman, B.; Solomon, E. I. *J. Am. Chem. Soc.* **2006**, *128*, 10442-10451.

- (39) Collman, J. P.; Gagne, R. R.; Reed, C. A.; Robinson, W. T.; Rodley, G. A. *Proc. Natl. Acad. Sci. U.S.A.* **1974**, *71*, 1326-1329.
- (40) Collman, J. P. *Acc. Chem. Res.* **1977**, *10*, 265-272.
- (41) Scheidt, W. R.; Osvath, S. R.; Lee, Y. J. *J. Am. Chem. Soc.* **1987**, *109*, 1958-1963.
- (42) DeBeer George, S.; Metz, M.; Szilagy, R. K.; Wang, H.; Cramer, S. P.; Lu, Y.; Tolman, W. B.; Hedman, B.; Hodgson, K. O.; Solomon, E. I. *J. Am. Chem. Soc.* **2001**, *123*, 5757-5767.
- (43) Yeh, J. J.; Lindau, I. *At. Data Nucl. Data Tables* **1985**, 1-155.
- (44) Hocking, R. K.; DeBeer George, S.; Gross, Z.; Walker, F. A.; Hodgson, K. O.; Hedman, B.; Solomon, E. I. *Inorg. Chem.* **2009**, *48*.
- (45) Dey, A.; Hocking, R. K.; Larsen, P.; Borovik, A. S.; Hodgson, K. O.; Hedman, B.; Solomon, E. I. *J. Am. Chem. Soc.* **2006**, *128*, 9825-9833.
- (46) Hocking, R. K.; DeBeer George, S.; Raymond, K. N.; Hodgson, K. O.; Hedman, B.; Solomon, E. I. *J. Am. Chem. Soc.* **2010**, *132*, 4006-4015.
- (47) Thole, B. T.; van der Laan, G.; Fuggle, J. C.; Sawatzky, G. A.; Karnatak, R. C.; Esteva, J.-M. *Phys. Rev. B.* **1985**, *32*, 5107-5118.
- (48) Cowan, R. D. *The Theory of Atomic Structure and Spectra*; University of California Press: Berkeley, 1981.
- (49) Butler, P. H. *Point Group Symmetry: Applications, Methods and Tables*; Plenum Press: New York, 1981.
- (50) Arrio, M.-A.; Sainctavit, P.; Cartier dit Moulin, C.; Mallah, T.; Verdaguer, M.; Pellegrin, E.; Chen, C. T. *J. Am. Chem. Soc.* **1996**, *118*, 6422-6427.
- (51) van der Laan, G.; Kirkman, I. W. *J. Phys: Condens. Matter* **1992**, *4*, 4189-4204.
- (52) Arrio, M.-A.; Sculler, A.; Sainctavit, P.; Cartier dit Moulin, C.; Mallah, T.; Verdaguer, M. *J. Am. Chem. Soc.* **1999**, *121*, 6414-6420.
- (53) Cartier dit Moulin, C.; Villain, F.; Bleuzen, A.; Arrio, M.-A.; Sainctavit, P.; Lomenech, C.; Escax, V.; Baudalet, F.; Dartyge, E.; Gallet, J.-J.; Verdaguer, M. *J. Am. Chem. Soc.* **2000**, *122*, 6653-6658.
- (54) Bianconi, A.; Della Longa, S.; Li, C.; Pompa, M.; Congiu-Castellano, A.; Udron, D.; Flank, A. M.; Lagarde, P. *Phys. Rev. B.* **1991**, *44*, 10126-10138.
- (55) De Groot, F. *Coord. Chem. Rev.* **2005**, *249*, 31-63.
- (56) Jianfeng, L.; Nair, S. M.; Noll, B. C.; Schultz, C. E.; Scheidt, W. R. *Inorg. Chem.* **2008**, *47*, 3841.
- (57) Jameson, G. B.; Rodley, G. A.; Robinson, W. T.; Gagne, R. R.; Reed, C. A.; Collman, J. P. *Inorg. Chem.* **1978**, *17*, 850-857.
- (58) Frisch, M. J.; et. al. *Gaussian 09*, Revision B.01; Gaussian Inc.: Wallingford, CT. See SI for full reference.
- (59) Becke, A. D. *Phys. Rev. A: Gen. Phys.* **83** **1988**, 3098-3100.
- (60) Perdew, J. P. *Phys. Rev. B: Condens. Matter* **33** **1986**, 8822-8824.
- (61) Baerends, E. J.; et al. *Amsterdam Density Functional*, SCM, Theoretical Chemistry, Vrije Universiteit, Amsterdam, The Netherlands, <http://www.scm.com>.
- (62) Tenderholt, A. L. *QMForge: A Program to Analyze Quantum Chemistry Calculations*, v. 2.1; Stanford University: Stanford, CA, 2007; <http://qmforge.sourceforge.net>.
- (63) Bergman, D. L.; Laaksonen, L.; Laaksonen, A. *J. Mol. Graph. Model.* **1997**, *15*, 301-306.
- (64) Laaksonen, L. *J. Mol. Graph.* **1998**, *10*, 33-34.
- (65) Jameson, G. B.; Molinaro, F. S.; Ibers, J. A.; Collman, J. P.; Brauman, J. I.; Rose, E.; Suslick, K. S. *J. Am. Chem. Soc.* **1980**, *102*, 3224-3237.
- (66) Park, S.-Y.; Yokoyama, T.; Shibayama, N.; Shiro, Y.; Tame, J. R. H. *J. Mol. Biol.* **2006**, *360*, 690-701.
- (67) Vojtěchovský, J.; Chu, K.; Berendzen, J.; Sweet, R. M.; Schlichting, I. *Biophys. J.* **1999**, *77*, 2153-2174.

**Table 1.** Summary of Iron L-edge Experimental Data.

Compound	Total Intensity	Total % Metal Character	L <sub>3</sub> /L <sub>2</sub> Maxima	L <sub>3</sub> Area	L <sub>2</sub> Area	Branching L <sub>3</sub> /(L <sub>2</sub> + L <sub>3</sub> )
[Fe <sup>II</sup> (pfp)(1-MeIm) <sub>2</sub> ]	38 (3)	302	708.2, 720.1	26.3	11.7	0.69
[Fe <sup>III</sup> (tpp)(ImH) <sub>2</sub> ]Cl	46 (3)	365	709.2, 721.3	30.8	15.2	0.67
[Fe <sup>II</sup> (pfp)]	40 (4)	318	708.1, 720.2	30.2	9.8	0.76
[Fe <sup>II</sup> (pfp)(1-MeIm)(CO)]	41 (4)	326	708.6, 720.7	27.8	13.2	0.68
[Fe(pfp)(1-MeIm)O <sub>2</sub> ]	39 (2)	310	708.3, 720.3	26.1	12.9	0.67

Total intensity is the integrated intensity of both the L<sub>3</sub>- and L<sub>2</sub>-edges. The total percent metal character represents the amount of d-character in the unoccupied orbitals and includes the effects of covalency and backbonding. Maxima given in eV at the energy of the L<sub>3</sub>- and L<sub>2</sub>-edge.

**Table 2.** Calculated First Shell Bond Lengths of Picket Fence Porphyrin Complexes.

Compound	Fe–Axial	Fe–Transaxial	Fe–Equatorial	Fe Out-of-Plane	Ref.
[Fe <sup>II</sup> (pfp)(1-MeIm) <sub>2</sub> ]	1.99 (2.00)	1.97 (1.99)	2.00 (1.99)	0.01 (0.00)	56
[Fe <sup>III</sup> (pfp)(1-MeIm) <sub>2</sub> ] <sup>+</sup>	2.00	1.97	1.99	0.01	
[Fe <sup>II</sup> (pfp)]	—	—	1.98	0.00	
[Fe <sup>II</sup> (pfp)(1-MeIm)(CO)]	1.73	2.06	2.01	0.05	
[Fe <sup>II</sup> (tpp)(ImH) <sub>2</sub> ]	1.97	1.97	2.00	0.00	
[Fe <sup>III</sup> (tpp)(ImH) <sub>2</sub> ] <sup>+</sup>	1.98 (1.96)	1.98 (1.96)	2.01 (1.99)	0.00 (0.00)	41

First shell bond lengths (Å) of geometry optimized structures (UPB86 with 6-311G\* on Fe, 6-31G\* on C, N, O, H). Measurements compared to crystal structure geometries, in parenthesis, where available. Fe–Axial refers to the picket substituted side of the porphyrin. Fe–Equatorial is an average of the four Fe–N heme bonds.

**Table 3.** Final VBCI Fit Parameters.

Compound	Crystal Field	Configuration Energies			Mixing Parameters ( <i>T</i> )				
	10Dq, Ds, Dt	Δ	Δ <sub>BB</sub>	Q–U	x <sup>2</sup> –y <sup>2</sup> ( <i>b</i> <sub>1g</sub> )	z <sup>2</sup> ( <i>a</i> <sub>1g</sub> )	xy ( <i>b</i> <sub>2g</sub> )	xz/yz ( <i>e</i> <sub>g</sub> )	xz/yz π*
[Fe <sup>II</sup> (pfp)(1-MeIm) <sub>2</sub> ]	2.40, 0.09, 0.07	–0.60	–1.65	1.2	2.15	1.80	0.50	1.50	0.65
[Fe <sup>III</sup> (tpp)(ImH) <sub>2</sub> ] <sup>+</sup>	2.65, 0.09, 0.08	–0.60	–1.00	1.2	2.85	2.50	1.00	1.50	1.00
[Fe <sup>II</sup> (pfp)]	2.30, 0.40, 0.10	–0.60	–0.60	1.2	2.15	0.50	0.50	0.85	0.20
[Fe <sup>II</sup> (pfp)(1-MeIm)(CO)]	2.50, 0.15, 0.02	–1.60	–2.90	1.0	2.15	2.25	0.50	2.80	1.80
[Fe(pfp)(1-MeIm)O <sub>2</sub> ]	2.40, 0.09, 0.05	–1.80	–2.25	1.1	2.15	1.95	0.50	2.10	1.00

Final fit parameters for the 2p<sup>6</sup> initial state and 2p<sup>5</sup> final state with a d<sup>6</sup> ground state configuration. *b*<sub>1g</sub>, *a*<sub>1g</sub>, *b*<sub>2g</sub>, and *e*<sub>g</sub> represent LMCT mixing parameters where π\* represents MLCT mixing. All other MLCT *T*s were set to zero.

**Table 4.** Comparison of Calculated and Experimental d-Characters in Valence Orbitals for Reference Complexes.

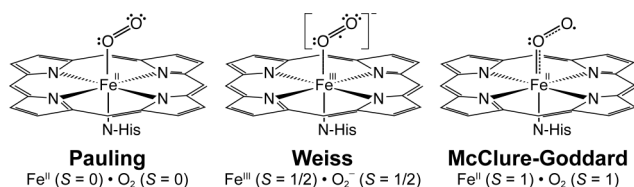
Compound	% Total Metal Character				VBCI (DFT) % Metal Character per Orbital (DOC)				
	TI	Intensity	VBCI	DFT	$x^2-y^2 (b_{1g})$	$z^2 (a_{1g})$	$xy (b_{2g})$	$xz/yz (e_g)$	$xz/yz \pi^*$
[Fe <sup>II</sup> (pfp)(1-MeIm) <sub>2</sub> ]	38 (3)	302	306	314	68 (68)	69 (69)	(90)	(71)	8 (10)
[Fe <sup>III</sup> (tpp)(ImH) <sub>2</sub> ] <sup>+</sup>	46 (3)	365	361	363	68 (67)	63 (67)	(90)	83 (71)	4 (6)
[Fe <sup>II</sup> (pfp)]	40 (4)	318	318	316	69 (67)	85 (83)	(90)	71 (83)	6 (4)
[Fe <sup>II</sup> (pfp)(1-MeIm)(CO)]	41 (4)	326	328	314	64 (62)	60 (57)	(93)	(56)	20 (19)

The percent metal character summed over the unoccupied orbitals reflects the combined effects of covalency and backbonding. TI = Total Intensity from the integrated L-edge spectrum. The projected VBCI values for each orbital symmetry are given along with the corresponding DFT values, where values for  $d_{xz}$ ,  $d_{yz}$ , and  $\pi^*$  orbitals are averaged for both  $\alpha$  and  $\beta$  spins to compare to the VBCI model in  $D_{4h}$  symmetry.

**Table 5.** Comparison of Calculated and Experimental Values for [Fe(pfp)(1-MeIm)O<sub>2</sub>].

	% Total Metal Character			% Metal Character per Orbital (DOC)				
	TI	Intensity	Total	$x^2-y^2 (b_{1g})$	$z^2 (a_{1g})$	$xy (b_{2g})$	$xz/yz (e_g)$	$xz/yz \pi^*$
[Fe(pfp)(1-MeIm)O <sub>2</sub> ]	39 (2)	310	306	67	64	—	—	11
DFT - Unpolarized	—	—	344	66	60	—	36	5
DFT - Polarized ( $\alpha/\beta$ )	—	—	342	65/64	62/57	—	57/11	9/4

The percent metal character summed over the unoccupied orbitals reflects the combined effects of donor and backbonding. TI = Total Intensity from the integrated normalized L-edge spectrum. Projected VBCI orbital covalencies for [Fe(pfp)(1-MeIm)O<sub>2</sub>] are from Figure 11. DFT values are based on Mulliken populations of the appropriate molecular orbitals.



**Scheme 1.** The three limiting descriptions of the Fe–O<sub>2</sub> bond. Pauling low-spin ( $S = 0$ ) Fe<sup>II</sup> singlet with singlet O<sub>2</sub>, Weiss low-spin doublet ( $S = 1/2$ ) Fe<sup>III</sup>, antiferromagnetically coupled to an O<sub>2</sub><sup>−</sup> doublet, or the McClure, Harcourt, and Goddard (Ozone model) of an intermediate-spin ( $S = 1$ ) Fe<sup>II</sup> triplet, antiferromagnetically coupled to triplet O<sub>2</sub>.

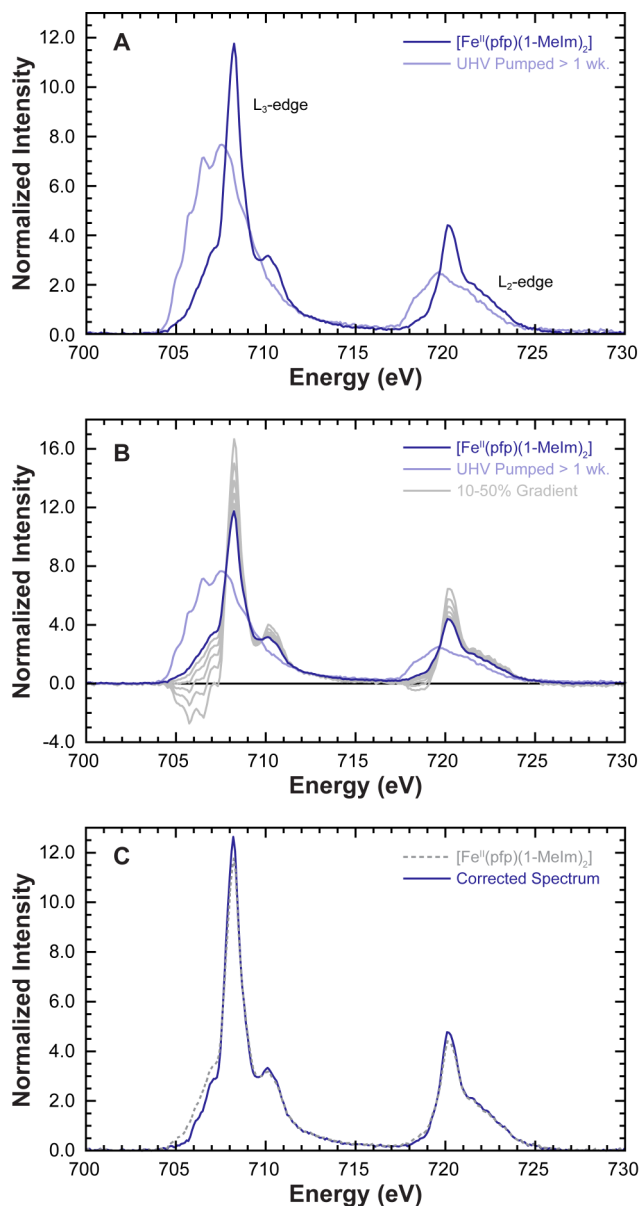


**Figure 1.** A: Normalized L-edge data for [Fe<sup>II</sup>(pfp)(1-MeIm)<sub>2</sub>] (blue) vs. the same sample pumped for one week under UHV conditions (light blue). B: Subtraction of “pumped” data and renormalization curves (grey) from 10–50% pumped contribution. C: Normalized L-edge data for [Fe<sup>II</sup>(pfp)(1-MeIm)<sub>2</sub>] (—) vs. the final corrected spectrum (---) with 15% pumped contribution removed.

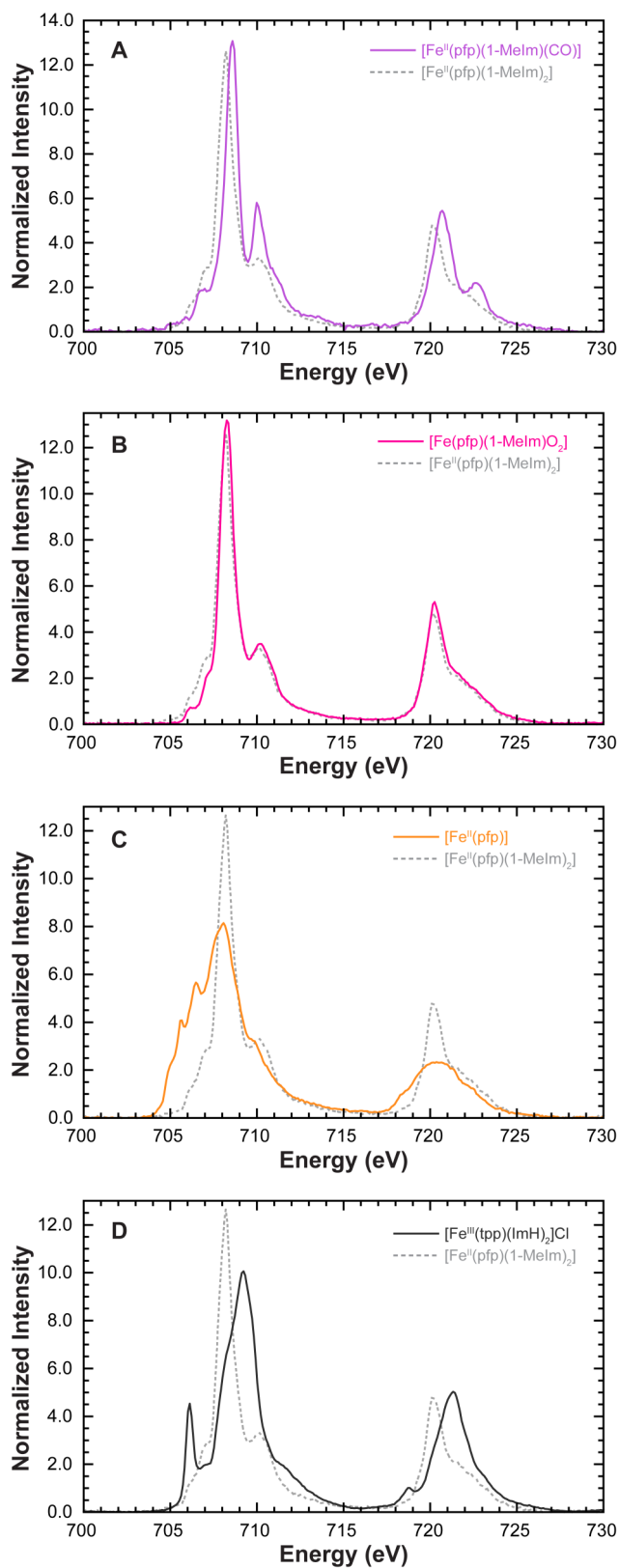


**Figure 2.** Panes A and B show the corrected L-edge spectra for low-spin ferrous  $[\text{Fe}^{\text{II}}(\text{pfp})(1\text{-MeIm})(\text{CO})]$  (> 20% pumped) and  $[\text{Fe}(\text{pfp})(1\text{-MeIm})(\text{O}_2)]$  (> 15% pumped) respectively. C: Intermediate spin ( $S = 1$ )  $[\text{Fe}^{\text{II}}(\text{pfp})]$ . D: Low-spin ferric ( $S = 1/2$ )  $[\text{Fe}^{\text{III}}(\text{tpp})(\text{ImH})_2]\text{Cl}$ . All panes plotted with the corrected L-edge spectrum of  $[\text{Fe}^{\text{II}}(\text{pfp})(1\text{-MeIm})_2]$  (----) as a reference.

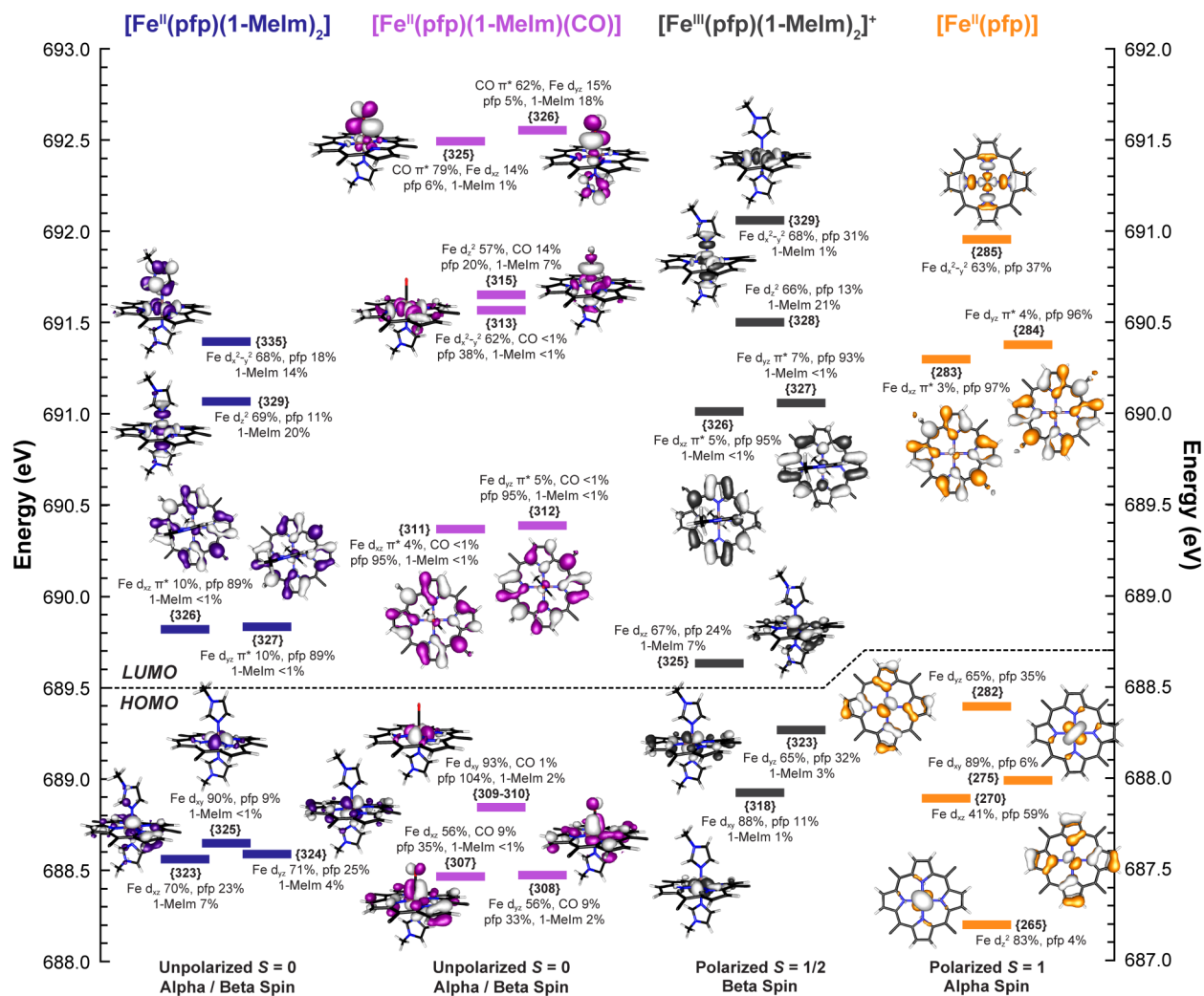


**Figure 3.** Comparison of the molecular orbitals for low-spin  $[\text{Fe}^{\text{II}}(\text{pfp})(1\text{-Melm})_2]$  (blue),  $[\text{Fe}^{\text{II}}(\text{pfp})(1\text{-Melm})(\text{CO})]$  (purple), and  $[\text{Fe}^{\text{III}}(\text{pfp})(1\text{-Melm})_2]^+$  (black) plotted on the left energy axis, with intermediate-spin ( $S=1$ ) ferrous  $[\text{Fe}^{\text{II}}(\text{pfp})]$  (orange) on the right axis. Orbitals are numbered according to the Gaussian output with the predominant fragment components in each molecular orbital listed above or below. Energy axes are shifted with the lowest energy Fe 2p orbital set to zero. For reference, the complete  $\alpha$  and  $\beta$  molecular orbitals of  $[\text{Fe}^{\text{III}}(\text{pfp})(1\text{-Melm})_2]^+$  and  $[\text{Fe}^{\text{II}}(\text{pfp})]$  are given in SI Figure S6. The picket porphyrin substituents have been removed for clarity but were included in all calculations. Orbitals are plotted with an isodensity value of  $\pm 0.03$ .

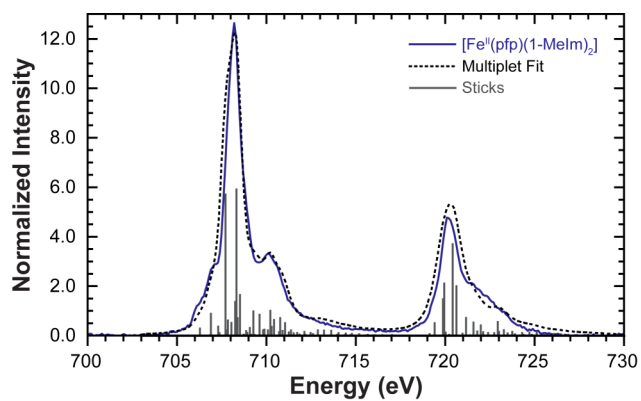


**Figure 4.** Final VBCI fit (----) for low-spin ferrous  $[\text{Fe}^{\text{II}}(\text{pfp})(1\text{-MeIm})_2]$ . The sticks represent the individual multiplet transitions that contribute to the simulated spectrum.

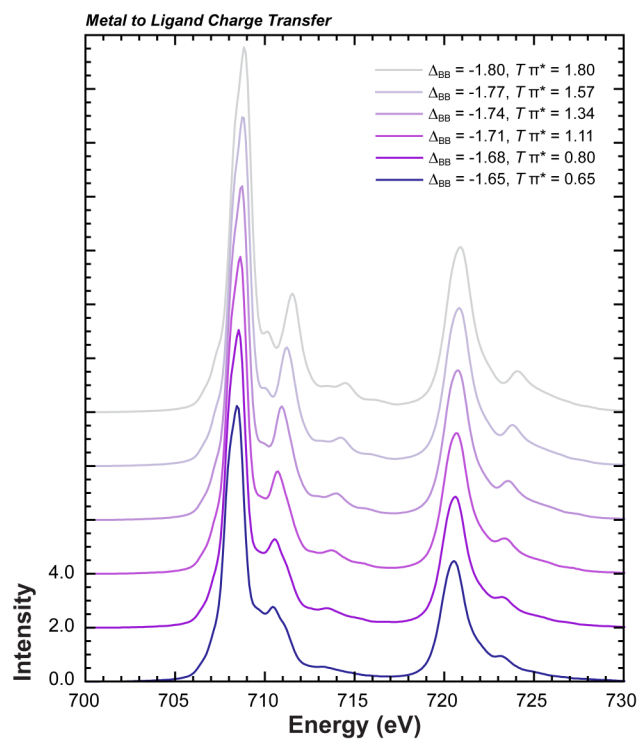


**Figure 5.** Systematic multiplet progression from  $[\text{Fe}^{\text{II}}(\text{pfp})(1\text{-MeIm})_2]$  to  $[\text{Fe}^{\text{II}}(\text{pfp})(1\text{-MeIm})(\text{CO})]$  that shows the effects of increased MLCT using both  $\Delta_{\text{BB}}$  and the  $\pi^*$  mixing parameter ( $T$ ).

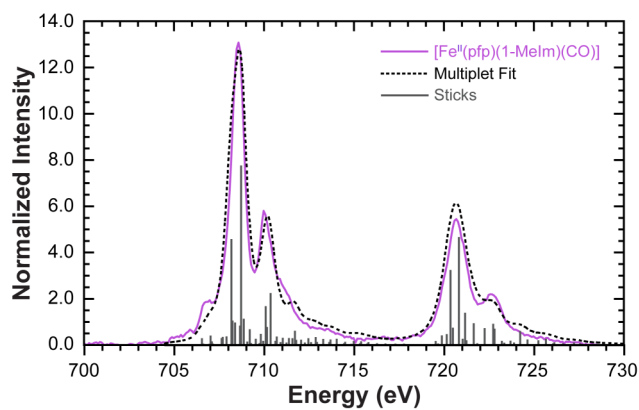


**Figure 6.** Final VBCI fit (----) for low-spin ferrous  $[\text{Fe}^{\text{II}}(\text{pfp})(1\text{-Melm})(\text{CO})]$ . The VBCI multiplet fit reproduces both the sharpening of the main  $L_3$ -edge feature and the addition of the high-energy feature at 710.0 eV associated with backbonding into the CO  $\pi^*$  orbitals.

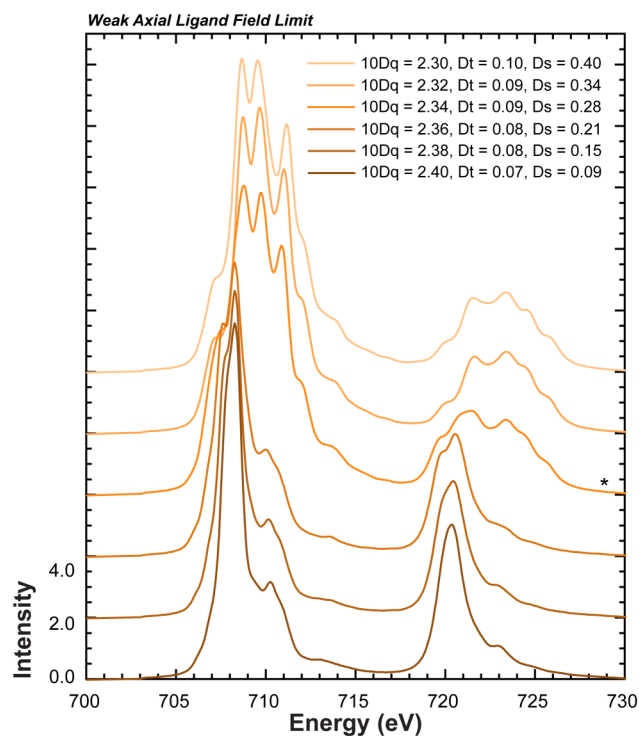


**Figure 7.** Systematic multiplet progression from low-spin ( $S = 0$ )  $[\text{Fe}^{\text{II}}(\text{pfp})(1\text{-Melm})_2]$  to intermediate-spin ( $S = 1$ ). The spin state change occurs between traces three and four, orange (\*), and results in the observed spectral broadening and three peak multiplet structure observed for  $[\text{Fe}^{\text{II}}(\text{pfp})]$ .

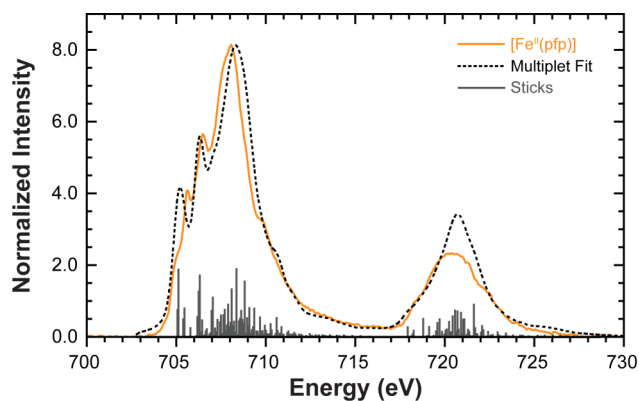


**Figure 8.** Final VBCI fit (----) for intermediate-spin ( $S = 1$ ) ferrous 4-coordinate  $[\text{Fe}^{\text{II}}(\text{pfp})]$ . The VBCI multiplet fit reproduces both the broadening of the main  $L_3$ -edge feature and the relative three feature  $L_3$ -edge structure.

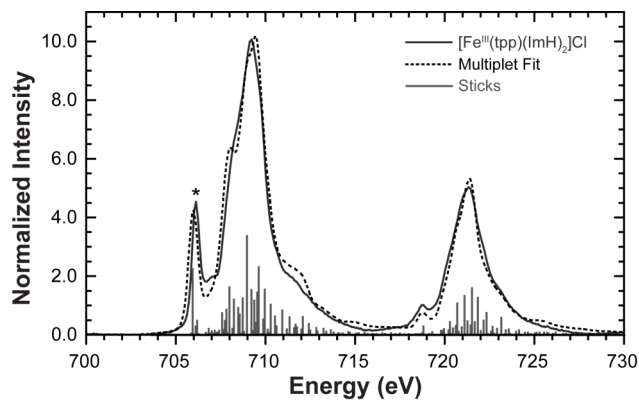


**Figure 9.** L-edge fit (----) to low-spin ( $S = 1/2$ ) ferric  $[\text{Fe}^{\text{III}}(\text{tp})(\text{ImH})_2]\text{Cl}$ . This fit reproduces the previous result<sup>36</sup> on low-spin ferric heme complexes where the presence of a  $d\pi$  hole (\*) increases the amount of  $\pi$ -donation from the heme and reduces the amount of MLCT backbonding into the porphyrin  $\pi^*$  orbitals.

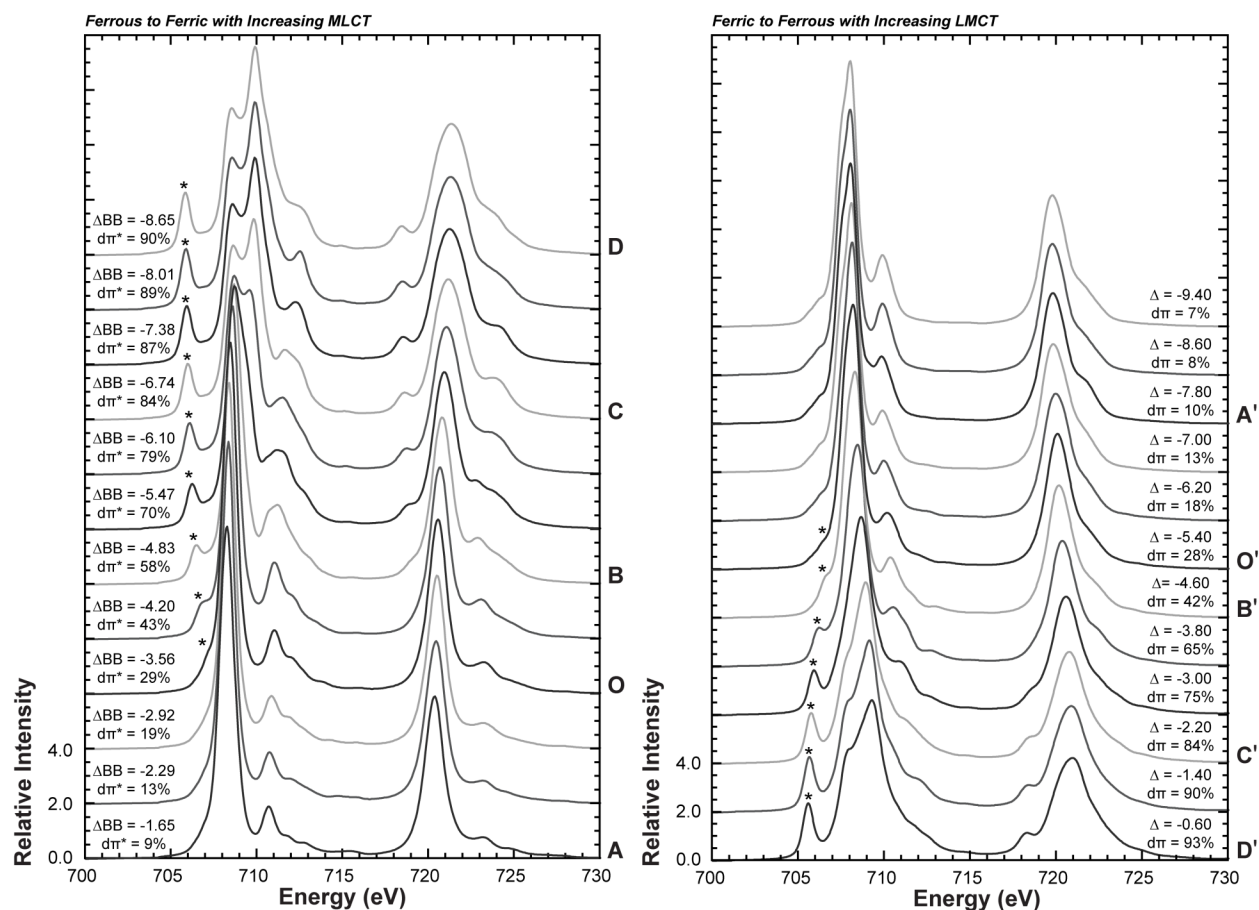


**Figure 10.** Left panel shows a systematic multiplet progression from a low-spin  $d^6$  with a  $\Delta_{BB} = -1.65$  eV to a low-spin  $d^5$  at  $\Delta_{BB} = -8.65$  eV resulting in progressively more MLCT from 9% to 90%  $d\pi^*$  hole character on the iron. The first trace, A, was generated using the same parameters used to fit  $[\text{Fe}^{\text{II}}(\text{pfp})(1\text{-MeIm})_2]$ , but with a larger ligand field splitting, which was required to maintain a low-spin configuration ( $10Dq = 3.30$ ,  $Dt = 0.01$ ). This additional progression can be found in SI Figure S8. The right panel shows a parallel series starting with the low-spin  $d^5$  parameters used to fit  $[\text{Fe}^{\text{III}}(\text{tpp})(\text{ImH})_2]\text{Cl}$  with progressively more LMCT into the  $d\pi$  hole yielding a simulation with predominantly low-spin  $d^6$  character. 3d spin-orbit coupling was set to zero in these simulations.

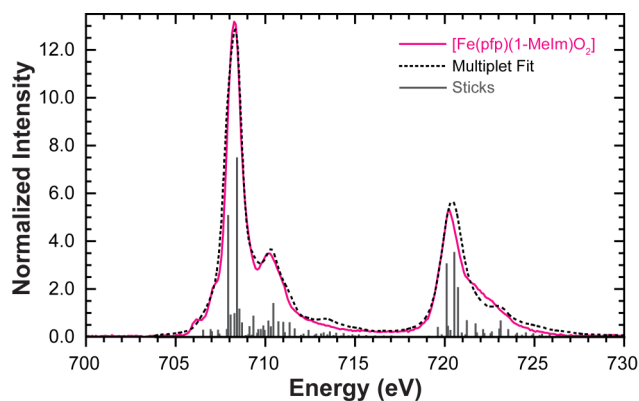


**Figure 11.** Final multiplet fit (----) to the L-edge spectrum of  $[\text{Fe}(\text{pfp})(1\text{-MeIm})\text{O}_2]$ . Fit generated using a three-configuration ( $d^{N-1}$ ,  $d^N$ ,  $d^{N+1}$ ) VBCI multiplet model including both MLCT and LMCT from a  $d^6$  ground state. The sticks represent the individual multiplet transitions that contribute to the simulated spectrum.

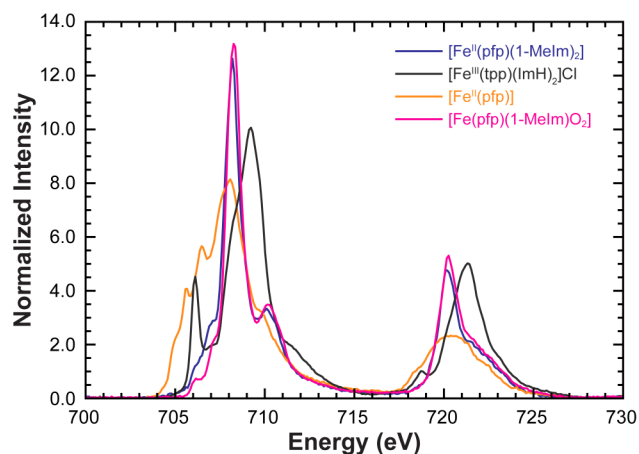


**Figure 12.** Overlay of the iron L-edge spectra of low-spin ferrous  $[\text{Fe}^{\text{II}}(\text{pfp})(1\text{-MeIm})_2]$  (blue), low-spin ferric  $[\text{Fe}^{\text{III}}(\text{tpp})(\text{ImH})_2]\text{Cl}$  (black), intermediate-spin ferrous  $[\text{Fe}^{\text{II}}(\text{pfp})]$  (orange), and low-spin  $[\text{Fe}(\text{pfp})(1\text{-MeIm})\text{O}_2]$  (magenta).

## TOC Graphic

